

Forward and inverse viscoelastic wave scattering by irregular inclusions for shear wave elastography

Simon Bernard and Guy Cloutier^{a)}

Laboratory of Biorheology and Medical Ultrasonics, University of Montréal Hospital Research Center (CRCHUM), 900 St-Denis, Suite R11.720, Montréal, Québec H2X 0A9, Canada

(Received 26 April 2017; revised 28 September 2017; accepted 1 October 2017; published online 26 October 2017)

Inversion methods in shear wave elastography use simplifying assumptions to recover the mechanical properties of soft tissues. Consequently, these methods suffer from artifacts when applied to media containing strong stiffness contrasts, and do not provide a map of the viscosity. In this work, the shear wave field recorded inside and around an inclusion was used to estimate the viscoelastic properties of the inclusion and surrounding medium, based on an inverse problem approach assuming local homogeneity of both media. An efficient semi-analytical method was developed to model the scattering of an elastic wave by an irregular inclusion, based on a decomposition of the field by Bessel functions and on a decomposition of the boundaries as Fourier series. This model was validated against finite element modeling. Shear waves were experimentally induced by acoustic radiation force in soft tissue phantoms containing stiff and soft inclusions, and the displacement field was imaged at a high frame rate using plane wave imaging. A nonlinear least-squares algorithm compared the model to the experimental data and adjusted the geometrical and mechanical parameters. The estimated shear storage and loss moduli were in good agreement with reference measurements, as well as the estimated inclusion shape. This approach provides an accurate estimation of geometry and viscoelastic properties for a single inclusion in a homogeneous background in the context of radiation force elastography. © 2017 Acoustical Society of America.

<https://doi.org/10.1121/1.5007729>

[KAW]

Pages: 2346–2364

I. INTRODUCTION

Elastography aims at measuring the local stiffness of biological tissues *in vivo*. Variations in tissue stiffness can indeed be indicative of pathologies, and are used for that reason in medicine through manual palpations. Elastography methods are developed to complement manual palpations with quantitative, reproducible, remote, and non-invasive stiffness measurements.^{1,2}

Elastography methods monitor the local mechanical properties of tissues from the observed motion. That motion can either be induced by manual compression, by natural movements of organs, or produced by the elastography method itself. Shear wave elastography (SWE) is based on the propagation of a shear wave, and relies on the equations of wave propagation to infer tissue properties. The present work lies in this framework. SWE uses the fact that the shear stiffness is several orders of magnitude smaller than the compression stiffness in soft biological tissues. Hence, shear waves propagate slowly (<10 m/s) compared to compression waves (typically 1540 m/s), and the shear wave propagation can be tracked using ultrasound,^{3,4} magnetic resonance,⁵ and optical imaging⁶ methods. With ultrasound, tracking of shear waves is possible using imaging at a high frame rate (a few kHz).

Shear waves can be generated using an exterior mechanical excitation,⁷ but this approach has been progressively replaced by excitation of shear waves within the tissue through ultrasound radiation force.^{3,8,9} Indeed, a long ultrasound push (hundreds of microseconds, compared to a few microseconds for imaging pulses) generates a radiation force strong enough to locally move the tissue by a few micrometers. This deformation then propagates as a shear wave. Acoustic radiation force imaging (ARFI) uses a single ultrasound push and infers locally the elastic properties from the time varying response of the tissue.³ Supersonic imaging (SSI) combines several successive pushes whose focus point is displaced at a velocity larger than the shear wave velocity to produce a conical shear wavefront that is perceived as a planar wavefront in the imaging plane.¹⁰ Very recently, shear waves could also be produced with a Lorentz force¹¹ and by laser under ablative and thermoelastic regimes.¹²

Two inverse problem approaches have been considered for shear wave elasticity assessment based on the assumption of isotropic linear tissues: the direct inversion (DI) method^{4,13–15} and the shear wave velocity technique.^{16–18} With both approaches, the shear stiffness μ is estimated as $\mu = \rho V_S^2$, where ρ is the density of the tissue and V_S is the shear wave speed. DI is based on the Helmholtz equation, which governs the shear wave propagation. This equation relates the second derivatives of the displacement field in space and time, with a proportionality factor depending on the shear wave velocity. The velocity can be obtained directly from the derivatives of the field. This method is sensitive to

^{a)}Also at: The Department of Radiology, Radio-Oncology and Nuclear Medicine, and Institute of Biomedical Engineering, University of Montréal, Montréal, Québec H3T 1J4, Canada. Electronic mail: guy.cloutier@umontreal.ca

noise due to the need to numerically differentiate the experimental displacement field. With the shear wave velocity technique, the shear wavefront in successive image frames is tracked using correlation or peak detection methods.¹⁹

An important limitation of the shear wave velocity approach described above is that it can only measure a single velocity of the propagating shear wave pulse (group velocity), while all biological tissues show some extent of velocity dispersion (i.e., a variation of the phase velocity with frequency) due to viscoelasticity.²⁰ Therefore, this method only partially characterizes the medium, reducing the complex behavior of the material to a single number. There is a growing set of evidence that viscoelasticity-related parameters are relevant for diagnosis, as exemplified using magnetic resonance elastography^{21,22} and ultrasound elastography.²³ Moreover, the shear wave velocity method is subject to artefacts in the case of strong contrast in elastic properties, due to the assumption of propagation in a single direction (i.e., neglecting refraction, diffraction, and reflection of the wave). These artefacts can be partially suppressed by the use of directional filters.²⁴

Recently, several approaches to extract the tissue viscosity from acoustic radiation force elastography data have been proposed. Chen *et al.*²⁵ and Defieux *et al.*²⁶ used the phase slope of the propagating shear wave to infer the phase velocity at various frequencies. In these studies, tissue stiffness and viscosity were deduced from a fitting of the velocity dispersion curve to a rheological model (usually the Voigt model). Several groups have proposed to measure the shear wave attenuation, which is a direct consequence of viscosity, using either diffraction correction methods,^{27,28} time-space Fourier analysis,²³ or a frequency shift modeling strategy.²⁹ These methods are, however, limited to homogeneous tissues and are not able to characterize the viscoelasticity of mechanical inclusions.

A strategy applicable to mechanical inclusions has been the modeling of the shear wave propagation and the use of the mechanical resonance phenomenon to deduce the viscoelasticity.³⁰ With this approach, the elasticity can be determined by the peak resonant frequencies and the viscosity by the bandwidth (i.e., quality factor) of those peaks. A successful inverse problem implementation based on this concept has been documented in the context of biogel characterization.³¹

Furthermore, inverse problem approaches considering more accurately the physics of the wave propagation have been proposed to characterize mechanical inclusions, such as the full waveform inversion.³² This numerically intensive approach originates from geophysics (see Ref. 33 for a recent review). To infer the internal structure of the Earth from recorded seismic signals, geophysicists are fitting a model to the recorded signals by adjusting the stiffness and mass density at every point of a given space grid. This results in a large and costly inverse problem solution, as the wave propagation problem is solved using a purely numerical method such as finite differences. Application of this approach on numerical elastography data has led to improvements in both accuracy and contrast of viscoelasticity measures.³²

By using the hypothesis of a localized heterogeneity in an otherwise homogeneous background, the complexity of

the previous approach can be considerably decreased, since a semi-analytical approach can be used instead of expensive purely numerical methods. Moreover, the size of the inverse problem is drastically reduced if piecewise continuous elastic moduli are considered (i.e., one modulus inside the inclusion and one outside). This approach was used by Montagnon *et al.*^{34,35} to infer the mechanical properties (stiffness and viscosity) of cylindrical and spherical inclusions in soft tissue phantoms from the scattering of an incident shear wave. An advantage of this approach is that the mechanical properties can be estimated independently at each frequency contained in the incident wave. The viscoelastic modulus of a sphere could be accurately measured over a large frequency bandwidth.³⁴ This method, however, suffers from several drawbacks hindering its practical application. First, it has been limited to canonical geometries [ellipse in two-dimensions (2D), sphere in three-dimensions (3D)], for which the scattering of an incident wave can be efficiently computed, but which may not accurately represent the reality (e.g., a lesion observed in breast cancer). Second, in the formulation of the inverse problem in the above cited works, the location and geometry of the inclusion had to be known *a priori*, and a small perturbation in one of these parameters could lead to dramatic perturbation of the estimated mechanical parameters.^{34,35}

The main objective of the present work was to overcome these two difficulties. First, a semi-analytical model of (visco)elastic wave scattering by cylindrical (2D) objects of irregular cross section was developed, with the aim to generalize the abovementioned models for elementary shapes.^{34,35} This model was validated against two-dimensional finite element modeling (2D FEM). Second, we conducted a set of experiments on soft tissue phantoms containing mechanical inclusions. The scattering model was used in an inverse problem formulation, in which the parameters of the inclusion and surrounding medium were optimized until the best match between experimental and predicted wave fields was obtained. Contrary to previous works, the geometry and location of the inclusion were not considered as *a priori* information, and parameters describing inclusion and surrounding medium properties within the ultrasound image were optimized along with their viscoelasticity values. This resulted in an inverse problem with a significantly higher number of parameters to be estimated, but which could still be solved using well-known gradient based iterative methods.

The paper is organized as follows. The theoretical modeling is presented in Sec. II, with a significant part of the equations reported in Appendixes A–C. In Sec. III, the choice of the truncation orders is discussed, using the elementary example of an off-centred circular cylinder. In Sec. IV, the comparison to 2D FEM is performed to validate the model for irregular inclusion shapes. Section V describes the experimental setup and the inverse problem. Results are presented and discussed in Sec. VI. Summary and conclusions are given in Sec. VII.

II. VISCOELASTIC WAVE SCATTERING MODEL

Scattering of acoustic or elastic waves by objects of simple geometry has been studied for a very long time,^{36–38} both

in 2D and 3D configurations. An efficient solution of the problem can be obtained by decomposition of the refracted and scattered wave fields as a series of Bessel and Hankel functions, and obtaining the coefficients of the series by imposing the appropriate boundary conditions at the interface between the inclusion and surrounding medium. This approach has been extended to irregular 2D shapes in acoustic scattering by Léon *et al.*³⁹ In this paper, this approach is generalized to elastic wave scattering. This is a significantly more complex situation because of the coupling between compression and shear waves.

Consider a viscoelastic cylinder of irregular cross section with a mass density ρ_1 , complex shear modulus μ_1 , and first Lamé coefficient λ_1 , embedded in a viscoelastic medium with a mass density ρ_2 , complex shear modulus μ_2 and first Lamé coefficient λ_2 (Fig. 1). The origin of the polar coordinate system (r, θ) is placed inside the cylinder. The boundary separating both media is described by the strictly positive and derivable function $R(\theta)$. The outer pointing normal of the contour is $\mathbf{n}(\theta) = n_r \mathbf{e}_r + n_\theta \mathbf{e}_\theta$. The displacement in the surrounding medium (medium 2) is the sum of the incident displacement \mathbf{u}_{inc} and the scattered displacement \mathbf{u}_2 . Displacement in the inclusion is the refracted displacement \mathbf{u}_1 . All three displacement fields are supposed to be constant along the z coordinate (it is a 2D problem) and harmonic, i.e., $\mathbf{u}(r, \theta, z, t) = \mathbf{u}(r, \theta) e^{i\omega t}$ (from now on, the time dependence is omitted). In addition, they satisfy the isotropic elastic wave equation

$$-\rho\omega^2 \mathbf{u} = (\lambda + 2\mu)\nabla(\nabla \cdot \mathbf{u}) + \mu\nabla \times \nabla \times \mathbf{u}. \quad (1)$$

According to the Helmholtz theorem, these three displacement fields can all be decomposed into three scalar potentials^{37,40}

$$\mathbf{u}(r, \theta) = \nabla\phi + \nabla \times \psi \mathbf{e}_z + a\nabla \times \nabla \times (\chi \mathbf{e}_z), \quad (2)$$

where each of the three potentials satisfies the Helmholtz equation, i.e.,

$$(\nabla^2 + K^2)\phi = 0 \quad \text{and} \quad (\nabla^2 + k^2)(\psi, \chi) = 0. \quad (3)$$

The factor a in Eq. (2) ensures the dimensional homogeneity of the equation, and the complex wave numbers K and k are related to the moduli through the dispersion relations

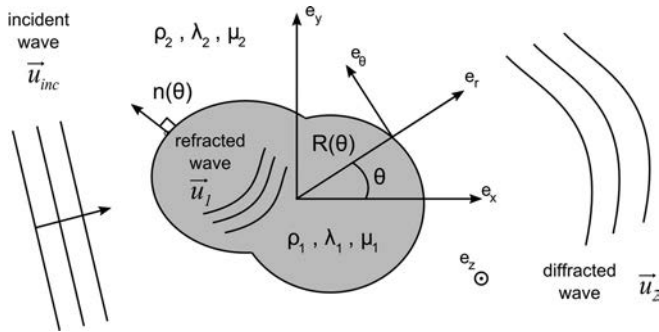


FIG. 1. Geometry of the problem. The inclusion is infinite in the z direction and the incident wave vector is contained in the (r, θ) plane.

$$K^2 = \frac{\rho\omega^2}{\lambda + 2\mu} \quad \text{and} \quad k^2 = \frac{\rho\omega^2}{\mu}. \quad (4)$$

The scalar potential ϕ is related to compressional waves, while the scalar potentials ψ and χ are related to shear waves whose polarization vectors are, respectively, orthogonal and collinear to the z axis.

Refracted and scattered wave fields are decomposed as sums of Bessel functions J_n (convergent) and Hankel functions of the first kind H_n^1 (divergent), which are solutions of the Helmholtz equation in cylindrical coordinates

$$\phi_1(r, \theta) = \sum_{n=-\infty}^{+\infty} A_n J_n(K_1 r) e^{in\theta}, \quad (5)$$

$$\psi_1(r, \theta) = \sum_{n=-\infty}^{+\infty} B_n J_n(k_1 r) e^{in\theta}, \quad (6)$$

$$\chi_1(r, \theta) = \sum_{n=-\infty}^{+\infty} C_n J_n(k_1 r) e^{in\theta}, \quad (7)$$

$$\phi_2(r, \theta) = \sum_{n=-\infty}^{+\infty} D_n H_n^1(K_2 r) e^{in\theta}, \quad (8)$$

$$\psi_2(r, \theta) = \sum_{n=-\infty}^{+\infty} E_n H_n^1(k_2 r) e^{in\theta}, \quad (9)$$

$$\chi_2(r, \theta) = \sum_{n=-\infty}^{+\infty} F_n H_n^1(k_2 r) e^{in\theta}. \quad (10)$$

To identify the coefficients A_n, B_n, C_n, D_n, E_n , and F_n in these decompositions, the boundary conditions at the interface $R(\theta)$ must be enforced. The continuity of the displacement vector at the interface is expressed as

$$\mathbf{u}_1(R(\theta), \theta) - \mathbf{u}_2(R(\theta), \theta) = \mathbf{u}_{\text{inc}}(R(\theta), \theta), \quad \forall \theta \in [0, 2\pi], \quad (11)$$

giving the three equations

$$\begin{aligned} u_1^r(\theta) - u_2^r(\theta) &= u_{\text{inc}}^r(\theta), \\ u_1^\theta(\theta) - u_2^\theta(\theta) &= u_{\text{inc}}^\theta(\theta), \\ u_1^z(\theta) - u_2^z(\theta) &= u_{\text{inc}}^z(\theta). \end{aligned} \quad (12)$$

Note that since the interface $R(\theta)$ is known and fixed, the fields on the boundary are functions of the single variable θ . The continuity of the surface tension vector $\mathbf{T} = \mathbf{n}(\theta) \cdot \boldsymbol{\sigma}$ at the interface $R(\theta)$, with $\boldsymbol{\sigma}$ the Cauchy stress tensor, gives the three following equations:

$$\begin{aligned} (\sigma_1^{rr} - \sigma_2^{rr})n_r + (\sigma_1^{r\theta} - \sigma_2^{r\theta})n_\theta &= \sigma_{\text{inc}}^{rr}n_r + \sigma_{\text{inc}}^{r\theta}n_\theta, \\ (\sigma_1^{\theta r} - \sigma_2^{\theta r})n_r + (\sigma_1^{\theta\theta} - \sigma_2^{\theta\theta})n_\theta &= \sigma_{\text{inc}}^{\theta r}n_r + \sigma_{\text{inc}}^{\theta\theta}n_\theta, \\ (\sigma_1^{zr} - \sigma_2^{zr})n_r + (\sigma_1^{z\theta} - \sigma_2^{z\theta})n_\theta &= \sigma_{\text{inc}}^{zr}n_r + \sigma_{\text{inc}}^{z\theta}n_\theta, \end{aligned} \quad (13)$$

where the dependence to the angular variable θ is implicit. The expressions of the displacement, stress, and strain field components as functions of the potentials ϕ, ψ , and χ are

given in [Appendix A](#). The expressions of the fields as functions of the decomposition coefficients A_n, B_n, C_n, D_n, E_n , and F_n can then be obtained by inserting Eqs. (5)–(10) into Eqs. (A1)–(A15). These expressions, together with some coefficients defined to simplify them, are given in [Appendix B](#).

As the interfaces considered in this study are irregular, the equations obtained by inserting the decompositions into the boundary conditions do not split into a linear system of equations, as is the case for a circular cylinder.^{36,38} Indeed, the fields have dependence to the angular variable θ . To obtain a system of linear equations that can be solved, this dependency must be suppressed. This can be achieved by decomposing the expression of the boundary conditions into Fourier series, as proposed by Léon *et al.*³⁹ For example, using expressions from [Appendix B](#), the continuity of the radial component of the displacement field,

$$u_1^r(\theta) - u_2^r(\theta) = u_{\text{inc}}^r(\theta), \quad (14)$$

becomes

$$\sum_{n=-\infty}^{+\infty} \sum_{q=-\infty}^{+\infty} \left[(A_n \beta_{n,q}^{L,1} - D_n \beta_{n,q}^{L,2}) + (B_n \alpha_{n,q}^{T,1} - E_n \alpha_{n,q}^{T,2}) \right] e^{iq\theta} = \sum_{q=-\infty}^{+\infty} u_q^r e^{iq\theta} \quad (15)$$

$$\begin{bmatrix} \beta_{n,p-n}^{L,1} & \alpha_{n,p-n}^{T,1} & 0 & -\beta_{n,p-n}^{L,2} & -\alpha_{n,p-n}^{T,2} & 0 \\ \alpha_{n,p-n}^{L,1} & -\beta_{n,p-n}^{T,1} & 0 & -\alpha_{n,p-n}^{L,2} & \beta_{n,p-n}^{T,2} & 0 \\ 0 & 0 & a\gamma_{n,p-n}^{T,1} & 0 & 0 & -a\gamma_{n,p-n}^{T,2} \\ \delta_{n,n-p}^1 & \varepsilon_{n,n-p}^1 & 0 & -\delta_{n,n-p}^2 & -\varepsilon_{n,n-p}^2 & 0 \\ \zeta_{n,n-p}^1 & \eta_{n,n-p}^1 & 0 & -\zeta_{n,n-p}^2 & -\eta_{n,n-p}^2 & 0 \\ 0 & 0 & a\kappa_{n,n-p}^1 & 0 & 0 & -a\kappa_{n,n-p}^2 \end{bmatrix} \cdot \begin{bmatrix} A_n \\ B_n \\ C_n \\ D_n \\ E_n \\ F_n \end{bmatrix} = \begin{bmatrix} u_p^r \\ u_p^\theta \\ u_p^z \\ \sigma_p^r \\ \sigma_p^\theta \\ \sigma_p^z \end{bmatrix}, \quad (19)$$

where the sub-matrices $\beta_{n,q}^{\tau,j}, \alpha_{n,q}^{\tau,j}, \gamma_{n,q}^{\tau,j}, \delta_{n,q}^j, \varepsilon_{n,q}^j, \zeta_{n,q}^j, \eta_{n,q}^j$, and $\kappa_{n,q}^j$ are of size $M \times N$ and contain the Fourier coefficients defined in [Appendix C](#), and the constant a was introduced in Eq. (2). The vectors A_n, B_n, C_n, D_n, E_n , and F_n (of size M), defined earlier, contain the unknown scattering coefficients while the right-hand side vector contains the information about the incident wave.

The linear system (19) splits into two uncoupled problems

$$\begin{bmatrix} \beta_{n,p-n}^{L,1} & \alpha_{n,p-n}^{T,1} & -\beta_{n,p-n}^{L,2} & -\alpha_{n,p-n}^{T,2} \\ \alpha_{n,p-n}^{L,1} & -\beta_{n,p-n}^{T,1} & -\alpha_{n,p-n}^{L,2} & \beta_{n,p-n}^{T,2} \\ \delta_{n,n-p}^1 & \varepsilon_{n,n-p}^1 & -\delta_{n,n-p}^2 & -\varepsilon_{n,n-p}^2 \\ \zeta_{n,n-p}^1 & \eta_{n,n-p}^1 & -\zeta_{n,n-p}^2 & -\eta_{n,n-p}^2 \end{bmatrix} \begin{bmatrix} A_n \\ B_n \\ D_n \\ E_n \end{bmatrix} = \begin{bmatrix} u_p^r \\ u_p^\theta \\ \sigma_p^r \\ \sigma_p^\theta \end{bmatrix} \quad (20)$$

and

with the Fourier coefficients $\beta_{n,q}^{L,j}, \alpha_{n,q}^{T,j}$, and u_q^r defined as

$$b_n^{\tau,j}(\theta) = \sum_{q=-\infty}^{+\infty} \beta_{n,q}^{\tau,j} e^{iq\theta} \quad \text{for } \tau = (L, T) \text{ and } j = (1, 2), \quad (16)$$

$$\frac{in}{R(\theta)} a_n^{\tau,j}(\theta) = \sum_{q=-\infty}^{+\infty} \alpha_{n,q}^{\tau,j} e^{iq\theta} \quad \text{for } \tau = (L, T), j = (1, 2), \quad (17)$$

and

$$u_{\text{inc}}^r(\theta) = \sum_{q=-\infty}^{+\infty} u_q^r e^{iq\theta}. \quad (18)$$

The other necessary Fourier coefficients are defined in [Appendix C](#). In the above notation, the superscript L refers to longitudinal waves and the superscript T refers to transverse waves.

All dependencies to the angular variable are included into the $e^{iq\theta}$ terms. Due to the orthogonality of $e^{iq\theta}$ functions, the boundary conditions then reduce to an infinite linear system of equations.³⁹ In practice, the decomposition into Bessel functions are truncated to an order M , and the Fourier series to an order N to get a finite system of equations described as

$$a \begin{bmatrix} \gamma_{n,p-n}^{T,1} & -\gamma_{n,p-n}^{T,2} \\ \kappa_{n,n-p}^1 & -\kappa_{n,n-p}^2 \end{bmatrix} \begin{bmatrix} C_n \\ F_n \end{bmatrix} = \begin{bmatrix} u_p^z \\ \sigma_p^z \end{bmatrix}. \quad (21)$$

This splitting occurs because we considered incident waves whose wave vector is contained in the (r, θ) plane (i.e., normal incidence on the cylinder). The sub-problem (20) concerns displacement contained in the (r, θ) plane, orthogonal to the cylinder axis (shear vertical SV waves and longitudinal waves), while the system (21) concerns only displacements polarized in the z direction, collinear to the cylinder axis (shear horizontal SH waves). In the case of an oblique incidence, the expressions given in [Appendixes A–C](#) would have contained additional terms from derivatives in the z direction, and the left matrix in the linear problem (19) would have been full.

If $M = N$, the linear systems are square and have exact solutions. If $N > M$, there are more equations than coefficients and the systems have a unique least-square solution.

For the incidence of acoustic wave on irregular cylinder, Léon *et al.*³⁹ only considered the case of $M = N$. We have, however, obtained better results with $N > M$, as shown in Sec. III. Once the scattering coefficients have been obtained, all the components of the displacement field can be computed everywhere in the (r, θ) plane using the expression given in Appendix A. The displacement was computed here on a regular Cartesian grid containing $N_x \times N_y$ points.

Although the model presented here is valid for the general case, the numerical examples and the experiments described in Secs. IV–VI are focusing on the case of soft solids, for which $\lambda \gg \mu$. Note also that, because of the frequency domain formulation, viscoelasticity is handled here simply by considering complex moduli (and, consequently, complex wave numbers and complex displacement fields).

III. SELECTING THE TRUNCATION ORDERS

In theory, the approximation of the wave field with a sum of Bessel (Hankel) functions can be made as accurate as desired by increasing the order of truncation M of the sum. However, in practice, high order functions cause numerical errors. Indeed, high order Bessel functions diverge rapidly as their argument grows, while Hankel functions are divergent close to the origin. Therefore, if the contour function $R(\theta)$ of the inclusion alternatively takes low and high values, the linear systems (20) and (21) are ill-conditioned. For that reason, it is not possible to arbitrarily increase the truncation number M when performing computation with a limited numerical precision (double precision in the present work), as the linear system to be inverted is becoming numerically singular. Additionally, in the method presented in Sec. II, a truncation order N for the Fourier series must also be selected, with the constraint $N \geq M$. In this section, numerical experiments studying the influence of the truncation numbers M and N on the accuracy of the results are reported.

A circle of radius R_0 whose centre is offset from the origin of the coordinate system by a distance b (relative to the radius R_0) along the x axis is described by

$$R(\theta) = R_0(b \cos \theta + \sqrt{1 - b^2(\sin \theta)^2}) \quad \text{for } b < 1. \quad (22)$$

This geometry is depicted in Fig. 2 for $R_0 = 1$. The solution of the scattering problem for an incident plane wave on such a cylinder with offset b , denoted $u^b(x, y)$, can be obtained from the method described here and compared to the solution, denoted $u^{\text{ref}}(x, y)$, of the simpler scattering problem for a centred circular cylinder,³⁶ previously implemented by our group.⁴¹ The two fields should be identical, up to a translation of the displacement fields of a distance b along the x axis. As b increases, the dynamic range of the function $R(\theta)$ also increases (Fig. 2), leading to more challenging numerical problems. It is therefore possible to evaluate the precision of the method by comparing results to the reference circular centred cylinder solution. For that purpose, we computed the root-mean-square error (RMSE),

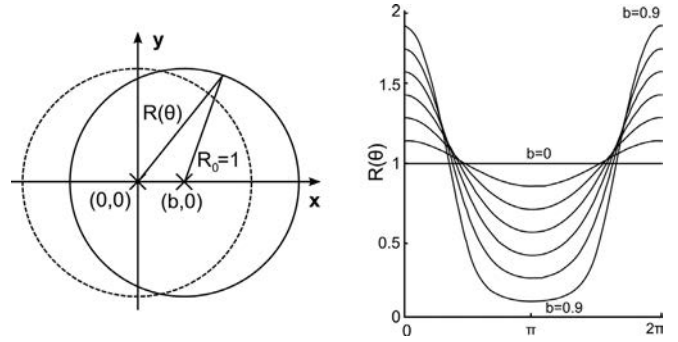


FIG. 2. Shifted cylinder geometry. As the relative shift b of the centre increases, the dynamic range of the contour function $R(\theta)$ also increases, leading to a more challenging numerical problem.

$$\text{RMSE} = 100 \times \sqrt{\frac{\sum_{i=1}^{N_x} \sum_{j=1}^{N_y} (u_{i,j}^{\text{ref}} - u_{i,j}^b)^2}{N_x \times N_y}} \quad (\text{in } \%) \quad (23)$$

over a $6 \times R_0$ by $6 \times R_0$ region centred on the cylinder with $N_x = N_y = 150$, for various incident frequencies as a function of the shift b , and for various choices of the truncation numbers N and M . As the Fourier series are computed using a fast Fourier transform algorithm, which work faster for powers of 2, we took N in the set [32, 64, 128, 256] while M was increased from 10 to 70 with a step of 10, with additional points at $M = N$ (at 32 and 64).

Computations were done for a soft solid (first Lamé coefficient $\lambda = 2.2 \text{ GPa} \gg \mu$) by considering a cylindrical geometry whose shear modulus (36 kPa) was three times larger than that of the surrounding medium (12 kPa). There was no contrast in the first Lamé coefficient and in the mass density ($\rho = 1000 \text{ kg m}^{-3}$). The incident shear wave was a unit amplitude plane wave propagating polarized along the y axis and propagating along the x axis. The incident frequency was determined by the non-dimensional product of the wave number $k = 2\pi/\lambda_{\text{shear}} = 2\pi f/V_S$ by the radius R_0 . Low kR_0 products ($=0.5$ here) correspond to small incident frequencies (shear wavelength λ_{shear} larger than the inclusion), while high kR_0 ($=10$ here) correspond to high frequencies (wavelength much smaller than the inclusion). The relative offset b ranged from 0.5 to 0.9. The mechanical contrast, inclusion size, and wave numbers used here are representative of the cases studied later.

The results are presented in Fig. 3 (left panel) for a large circle offset ($b=0.7$) and a moderately high incident frequency ($kR_0 = 5$) as a function of the truncation orders M and N . It can be observed that for every Fourier truncation number N , the error reaches a minimum for $M < N$. We also see that the minimum decreased when increasing N , except for $N = 256$, and that it was obtained for larger M . A similar behavior was observed for other incident frequencies and offsets b (not shown). For all tested numbers N , the numerical problem became singular for $M > 70$. From that experiment, the best choice for the truncation appeared to be $M = 40$ and $N = 128$. These numbers were used in the remainder of the paper.

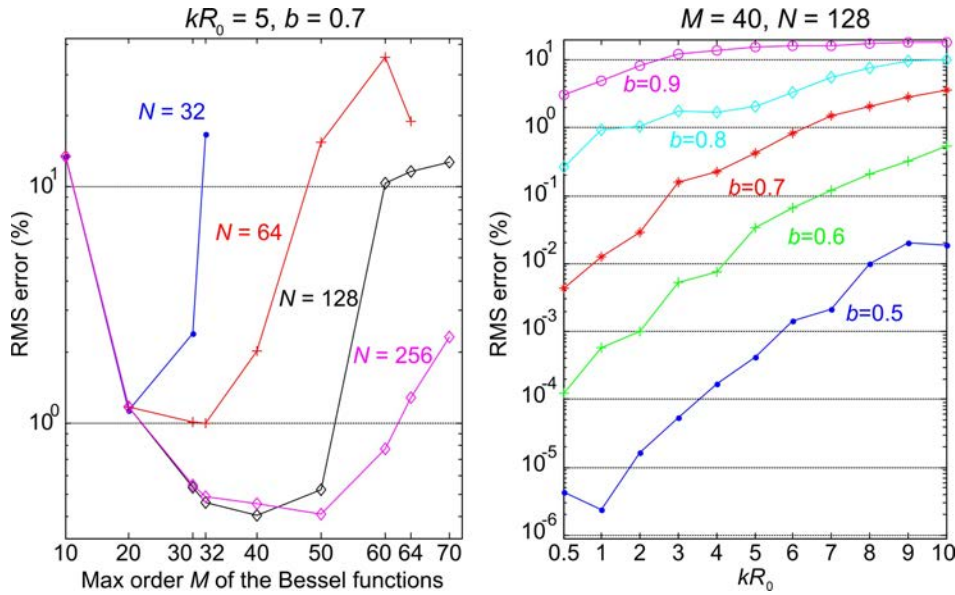


FIG. 3. (Color online) RMSE, relative to the incident wave amplitude, for computing the scattered field of a shifted cylindrical cylinder (depicted in Fig. 2). The left panel shows the error as a function of the truncation orders M and N , for a fixed incident wave number kR_0 and position shift b . In that configuration, the best results are obtained for $M = 40$ and $N = 128$. The right panel shows the error as a function of b and kR_0 for truncation orders fixed to these values.

In Fig. 3 (right panel), the results are presented as a function of b and kR_0 for fixed $M = 40$ and $N = 128$. The error increases as the incident frequency increases (higher kR_0) and as the shift b increases. This is expected, as higher frequencies imply more rapid spatial variations of the wave field and, therefore, this requires higher orders of Bessel (Hankel) functions, and because an increase in b leads to larger and more abrupt variations in the contour function $R(\theta)$. It can be observed, however, that good performances ($RMSE < 1\%$) are obtained at all frequencies for $b = 0.5$ and $b = 0.6$, and up to $kR_0 = 5$ for $b = 0.7$. For very large offsets ($b = 0.8$ and 0.9), the error is larger than 1% for all incident frequencies, and became $>10\%$ for the highest frequencies. This result highlights the limits of the proposed approach, which are reached for shapes that are very far from a circular cylinder and at high frequencies. The case explored here is, however, extreme and it is likely that variations in the contour function $R(\theta)$ will be smaller and smoother for many practical situations. Similar limits have been observed for the original method for acoustic scattering prediction³⁹ when applied to ellipses of high aspect ratios.⁴² As in our case, the dynamic range of the Bessel and Hankel functions evaluated on the contour rapidly exceeds the range of double precision numerical computations, and the problem becomes ill-conditioned or singular. A solution proposed by Cassereau *et al.*⁴² is to perform the computation with arbitrary numerical precision, which allows to set an arbitrarily high truncation order M at the cost of an increased computation cost. This approach was not explored here, as all examples presented in the rest of the paper are far from the numerical limits.

IV. FINITE ELEMENT VALIDATION OF THE FORWARD PROBLEM

Validation for non-canonical shapes was done using finite element modeling (FEM) of the scattering of an incident shear wave by cylinders of irregular cross section (structural mechanics module, version 3.3, COMSOL,

France). The case of a SV wave [polarization vector contained in the (x,y) plane and oriented along y] was considered, and simulations were performed in the frequency domain, i.e., assuming a harmonic excitation and, consequently, a harmonic displacement field.

The geometry of the numerical computation is described in Fig. 4. The complete mesh had a dimension of $14 \lambda_{\text{shear}}$ in width by $16 \times \lambda_{\text{shear}}$ in depth (the wavelength being calculated here for the background material). Absorbing regions of $2 \times \lambda_{\text{shear}}$ in width were defined on the edges of the mesh using the perfectly matched layers (PMLs) provided by the software to approximate an infinite medium. A prescribed displacement u_y in the y -direction was applied on the left edge of the mesh to generate the incident wave. This displacement was constant over the depth of the central box and then decreased toward 0 in the top and bottom absorbing regions to reduce edge effects. A triangular mesh was automatically generated, with about eight

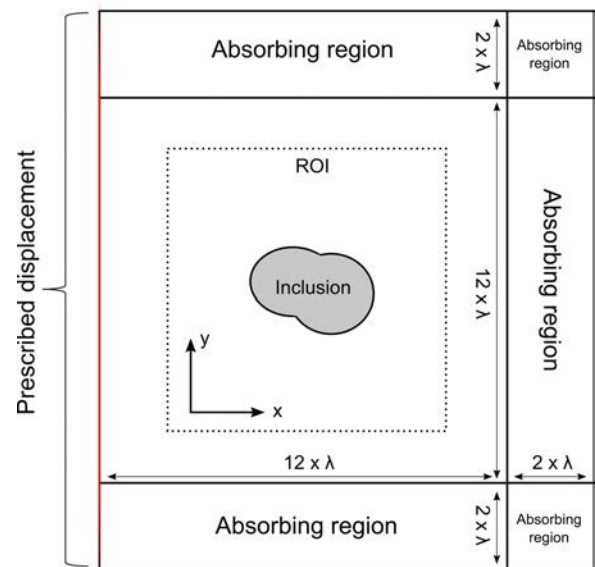


FIG. 4. (Color online) Setup for the FEM computation.

elements per wavelength, resulting in about 300 000 degrees of freedom in total.

A bean-shaped inclusion was obtained from

$$R(\theta) = R_0 \left(1 + \frac{\cos \theta}{6} + \frac{\sin 2\theta}{3} \right), \quad (24)$$

and a star-shaped inclusion was modeled using

$$R(\theta) = R_0 \left(1 + \frac{\cos 5\theta}{10} + \frac{\sin 5\theta}{10} \right). \quad (25)$$

For both shapes, an incident wave with a wave-number/radius product $kR_0 = 5$ and two elasticity contrasts were studied. In one case, the inclusion was three times softer than the surrounding medium, and in the other case it is three times harder. For all simulations, an imaginary part equal to 10% of the real part was added to the shear modulus of the inclusion and of the surrounding medium to introduce attenuation. This 10% value approximately corresponds to values observed experimentally in phantom experiments (see Sec. VI). No imaginary part was added to the first Lamé coefficient. Because the wavelength of compression waves is much larger than the observed propagation distance, the viscous effect on these waves was considered negligible. The amplitude of the displacement prescribed on the boundary was set so that the incident wave had unit amplitude at the entry of the $6R_0 \times 6R_0$ central square region-of-interest (ROI). The parameters of the FEM simulation are summarized in Table I.

The FEM-computed displacement fields were interpolated on a regular grid over the ROI for direct comparison with the semi-analytical approach. The RMSE over the ROI was calculated for the x - and y -displacement fields, with Eq. (23), except that the difference was calculated here between the FEM and the semi-analytical solutions.

Results are summarized in Table II. The RMSE are given in percentage of the incident wave amplitude. Errors were lower than 0.3% for both geometries and both contrasts (hard and soft), in the x - and y -polarized fields. The displacement fields are plotted for the stiff bean-shaped inclusion in Fig. 5. The differences between the two methods are not visible and the difference curves in the bottom panels were magnified 100 times for visibility. The very small errors are likely due to differences in boundary conditions. Indeed, the

TABLE I. Parameters of the FEM simulations.

First Lamé parameter	2.2 GPa
Mass density	1000 kg m ⁻³
Frequency	500 Hz
Size of the inclusion	$R_0 \approx 5.5$ mm ($kR_0 = 5$)
Inclusion shear modulus (soft)	$4 + 0.4i$ kPa
Inclusion shear modulus (hard)	$36 + 3.6i$ kPa
Surrounding medium shear modulus	$12 + 1.2i$ kPa
ROI size	$6R_0 \times 6R_0$
Width of the absorbing regions	$2 \lambda_{\text{shear}}$
Central box size	$12 \lambda_{\text{shear}}$
Element size	$\approx \lambda_{\text{shear}}/8$

TABLE II. RMSEs between the FEM computed displacement fields and the displacement fields given by the semi-analytical method, for the irregular inclusions modeled by Eqs. (24) and (25).

	RMSE, soft inclusion (%)		RMSE, hard inclusion (%)	
	x -polarization	y -polarization	x -polarization	y -polarization
Bean	0.07	0.21	0.05	0.22
Star	0.17	0.28	0.10	0.24

semi-analytical method considers a perfectly infinite medium, while it is only approximately obtained in the FEM model.

V. EXPERIMENTS AND INVERSE PROBLEM

A. Phantom preparation

Two phantoms were prepared containing each a cylindrical inclusion with an irregular cross section, as described by Eqs. (24) and (25) with $R_0 = 5$ mm. They were made from mixtures of agar (A9799, Sigma–Aldrich Chemical, St Louis, MO), gelatin (G2500, Sigma–Aldrich Chemical), and degassed water. The agar/gelatin concentrations, listed in Table III, were varied to obtain the desired contrasts in viscoelasticity moduli. The bean-shaped inclusion was stiffer than the surrounding medium, and the star-shaped inclusion was softer. A few milligrams of graphite powder was added to the inclusions (282863, Sigma–Aldrich chemical) to create a visual contrast to facilitate the positioning of the ultrasound probe.

Water was first heated to 70 °C and mixed with the gelatin powder. The mixture was cooled down to 50 °C, and the agar and graphite powder were added. At this temperature, the agar powder did not melt, creating a suspension of agar particles in a gelatin background. These particles acted as acoustic scatterers. The mixture was cooled down to 25 °C before casting it into rectangular molds of dimensions $12 \times 12 \times 7$ cm³. Acoustic windows were created in the mold to allow positioning the ultrasound probe (Fig. 6). To produce inclusion geometries, two 15-cm-long cylinders with the desired cross sections were 3D-printed (Dimension Elite, Stratasys, Eden Prairie, MN), and fixed horizontally in the rectangular molds at ~ 3 cm of the surface. The mixture for the surrounding material was casted around the cylinder, and stored at 4 °C for 6 h. The plastic cylinder was then carefully removed from the stiffened phantom, and the material used to produce the soft and hard inclusions was casted into the hole. The phantoms were stored at 4 °C overnight. Mixtures prepared for inclusions were also casted as homogeneous phantoms in other molds for reference measurements.

B. Data acquisition

The experimental setup for data acquisition is illustrated in Fig. 6. The incident shear wave was generated in a SSI-like configuration,^{10,16} from three radiation force pushes located at depths of 25, 30, and 35 mm. Each push was created by a 240- μ s-long excitation at a central frequency of

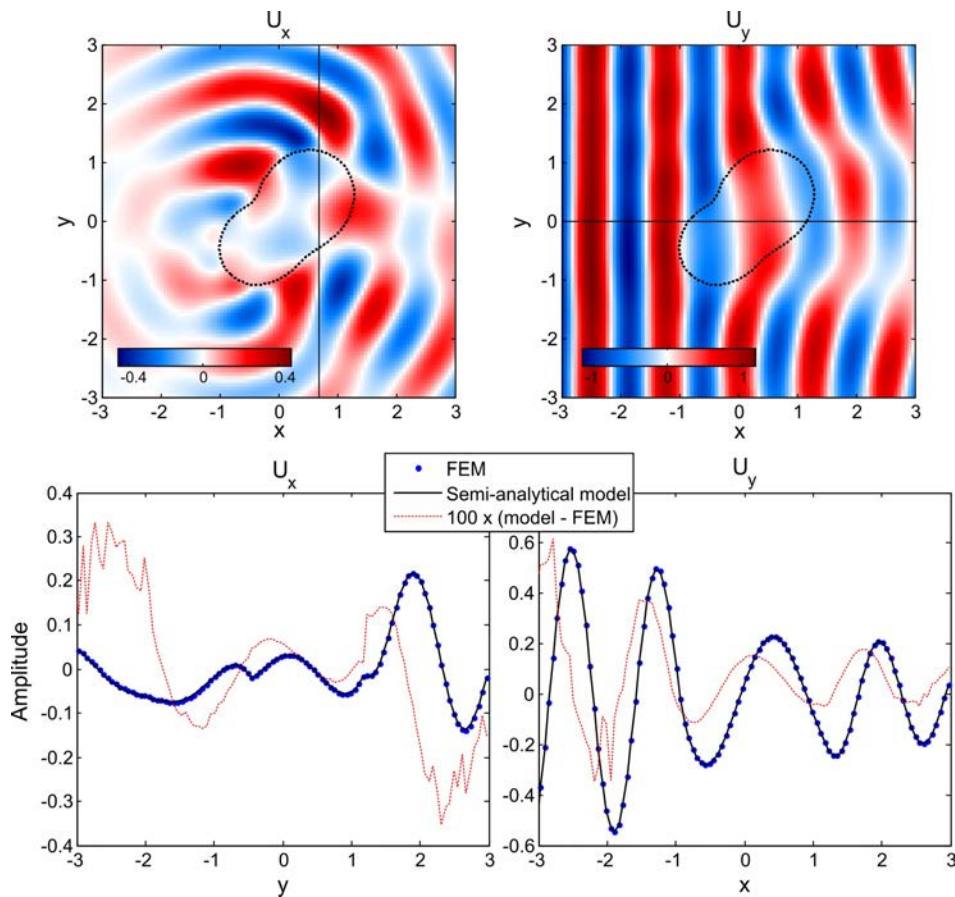


FIG. 5. (Color online) Validation of the semi-analytical elastic wave scattering model against FEM for the stiff bean-shaped inclusion. Top row shows the x axis (left) and y axis (right) polarized components of the stationary displacement fields at 500 Hz. The profiles along the solid black lines are plotted in the bottom row (blue dots), with the corresponding profiles from FEM (solid black lines superimposed on the blue dots). The difference between displacement curves is plotted with a $100\times$ magnification (dashed red line).

4.09 MHz, with a $20\ \mu\text{s}$ waiting time between two successive pushes at different depths. They were obtained by focusing the 40 left sided elements of a 128-element linear ultrasound probe [ATL L7-4 (Philips Healthcare, Bothell, WA), central frequency 5 MHz], on a research echograph (model V1, Verasonics, Kirkland, WA). Immediately after the pushing sequence, the probe was switched to the imaging mode and used to send short pulses on all elements to produce plane waves. Angle compounding was used to increase the image quality.⁴³ Plane waves tilted at four angles (-3° , -1° , 1° , and 3°) were successively sent at a 10 kHz frame rate during 28 ms. The echoes were beamformed in post-processing using a Fourier method,⁴⁴ and images obtained at the four angles were coherently summed, resulting in an effective frame rate of 2.5 kHz. A Doppler estimator⁴⁵ was used to track the displacement of speckle between two successive frames along the ultrasound beam direction (y -direction), and we therefore got a movie of the particle velocity field (displacement between frames and not with respect to an absolute reference).

As it is difficult to estimate the lateral motion from ultrasound echoes, a second probe (ATL L7-4, again) was

placed orthogonally to the first one. Immediately after the first sequence was completed (pushing + imaging), a second sequence was started in which the pushing was still done with probe #1, but the system then switched the active probe #2 to perform imaging. These echoes were beamformed similarly, and the particle velocity in the x -direction was then obtained from the same motion estimator. This setup allowed recording both polarizations of the field generated by the same pushing sequence. As the lateral polarization (probe #2) is usually not available in SWE experiments, it has not been used in the inverse problem, but utilized for a *posteriori* cross-validation of the model and estimated parameters.

The ROI for data analysis (Fig. 6) was 20 mm in width and 40 mm in depth. It was set to exclude the region where the push is generated. During the acquisition, the probe was placed so that the inclusion ROI was included in the image. A Fourier transform of the transient movies, from time to frequency domain, was done for each pixel of the movies to obtain maps of the stationary particle velocity fields (Fig. 6) using the fast Fourier transform algorithm. For this operation, 64 time samples were used (from 0 to $25.2\ \mu\text{s}$, which was sufficient to capture the entire time signal), providing stationary maps for frequencies in the range of 0–1250 Hz with a 39-Hz resolution.

TABLE III. Agar, gelatin, and graphite powder concentrations used in the preparation of phantoms.

	Agar	Gelatin	Graphite
Surrounding media	4%	4%	0%
Soft inclusion	1%	4%	0.1%
Hard inclusion	1%	15%	0.1%

C. Reference measurements

Reference SWE measurements were performed in the homogeneous phantoms prepared with the materials used for the inclusions, as well as in a homogeneous part of the

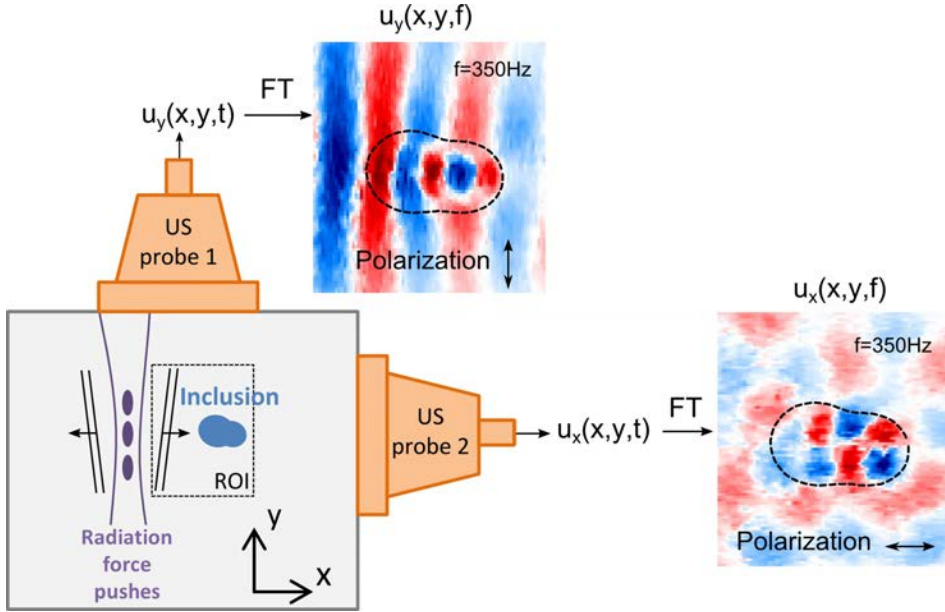


FIG. 6. (Color online) Experimental setup used for the scattered wave field measurements. A shear wave polarized along the y axis was generated with three radiation pushes emitted by probe #1. This same probe was used to image the y axis component of the wave field, while probe #2 imaged the x axis component. The recorded transient fields $u_x(x, y, t)$ and $u_y(x, y, t)$ were Fourier transformed from time to frequency domain at each pixel to produce stationary maps at frequencies ranging from 0 to 1250 Hz.

surrounding medium (i.e., far from the inclusion). The phase velocity as a function of frequency as well as the linear shear wave attenuation coefficient, defined as the slope of the attenuation vs frequency curve, were extracted from the data.

The wave velocity was measured at each frequency from a linear fit of the phase vs propagation distance using the shear wave spectroscopy method,²⁶ while the linear attenuation coefficient was obtained with a frequency shift method.²⁹ This latter algorithm assumes that the attenuation increases linearly with frequency, which is an appropriate assumption for agar-gelatin phantoms,²⁹ and extracts the attenuation coefficient from the decrease in the central frequency of the wave as it travels away from the source. Shear storage (μ') and loss (μ'') moduli could then be calculated at each frequency from the wave velocity $c(\omega)$ and linear attenuation coefficient α_0 with the relations

$$\mu'(\omega) = \rho\omega \frac{\left(\frac{\omega}{c(\omega)}\right)^2 - (\alpha_0\omega)^2}{\left[\left(\frac{\omega}{c(\omega)}\right)^2 + (\alpha_0\omega)^2\right]^2} \quad (26)$$

and

$$\mu''(\omega) = 2\rho\omega \frac{\frac{\omega}{c(\omega)} \times \alpha_0\omega}{\left[\left(\frac{\omega}{c(\omega)}\right)^2 + (\alpha_0\omega)^2\right]^2}. \quad (27)$$

These relations were obtained from the dispersion relation $k^2 = \rho\omega^2/\mu$, assuming $k = \omega/c(\omega) - i\alpha_0\omega$, and finally separating the real (μ') and imaginary (μ'') parts of the shear modulus.

D. Elasticity maps from the time-of-flight method

The shear wave data were also processed using the time-of-flight (TOF) method¹⁶ to compare its ability to

evaluate the inclusion geometry and elasticity compared to the inverse problem approach based on the scattering model developed here. First, a directional filter was applied to keep only the forward (left to right) propagating shear wave, and therefore to get rid of the reflected wave for reducing artefacts in reconstructed images.²⁴ Then, a time-to-peak (TTP) method was used to estimate the velocity of the forward propagating wave. The arrival time of the waveform maximum was estimated at each lateral position away from the push location. The velocity was then obtained as the inverse of the slope of the arrival time vs lateral position. A kernel size of 6 lateral pixel widths (about 1.8 mm) was used for the slope estimation. Before velocity estimation, the signals were averaged in the depth direction over 0.3 mm (8 pixels) to improve the signal-to-noise ratio, and interpolated from 2.5 kHz to 50 kHz for accurate estimation of TTP. Finally, a 3×3 pixel median filter was applied to the velocity images. Elasticity maps were obtained with the relation $\mu = \rho V_S^2$ with ρ fixed at 1000 kg m^{-3} . As the method was applied on the particle velocity field (see Sec. VB) and not the displacement field, it corresponds to the time-to-peak-slope (TTPS) method.¹⁹

E. Inverse problem formulation

The inverse problem was based on the wave velocity $c(f)$ and attenuation coefficient α_0 . That way, the linear dependency of the attenuation was automatically imposed to constraint the problem, while it would be difficult to do so with a parametrization using the shear storage and loss moduli. No constraint, however, was put on the wave velocity dependency with frequency, so that there were $2 \times N$ unknown velocities $c(f_n)$ (surrounding medium and inclusion), for the N discrete frequencies f_1, \dots, f_N in the frequency band of analysis.

The unknown geometry was represented by a Fourier series with a fixed order Q ,

$$R(\theta) = R_0 + \sum_{q=1}^Q a_q \cos(q\theta) + b_q \sin(q\theta). \quad (28)$$

This contour was defined in an arbitrary coordinate system whose position relative to the fixed coordinate system defined by the probe was parametrized by two additional unknown parameters x_0 and y_0 . The incident wave was a plane shear wave polarized in the y -direction with an unknown incidence angle ϕ (see Fig. 6), and unknown phase $\varphi(f)$ and amplitude $A(f)$ at each frequency.

All estimated parameters were grouped into the vector \mathbf{p} . The cost function to be minimized was the squared norm of the difference between the (complex) experimental and predicted stationary velocity fields, summed over all pixels of the ROI, and all discrete frequencies inside the frequency band of analysis

$$\mathbf{p} = \operatorname{argmin} \left[\sum_{f=f_1}^{f_n} \sum_{i=1}^{N_x} \sum_{j=1}^{N_y} |v_{i,j,f}^{\text{exp}} - v_{i,j,f}^{\text{calc}}(\mathbf{p})|^2 \right]. \quad (29)$$

The non-linear Levenberg-Marquardt unconstrained minimization algorithm was used. The partial derivatives of the cost function were obtained at each iteration of the algorithm by a finite-difference approximation. For the initialization, mean shear wave velocity values roughly evaluated with the TOF method (Sec. VD) inside and outside the inclusion were used. The inclusion geometry was initialized with a circle of 5-mm radius (i.e., $R_0 = 5$ mm, $a_m = 0$, and $b_m = 0$, $\forall m$ placed in the middle of the ROI).

A correction factor was applied to the data to compensate for the cylindrical diffraction, due to the actual shape of the source that was not modeled by the 2D problem. Experimental data were multiplied by a \sqrt{r} factor, where r is the distance from the focus line of the acoustic radiation force push. Without this correction, the inversion algorithm would artificially increase the attenuation to compensate for the decrease in amplitude due to diffraction.³⁵

Note that the model described above (Sec. II) was written for the displacement field u , while the experimental data correspond to particle velocity field v (Sec. VB). This is not a problem here, since in the frequency domain these two quantities are simply related by an $i\omega$ factor. As the amplitude and phase of the incident wave at each frequency were free parameters in the inversion, the complex proportionality factor was automatically included in the fitted phase and amplitude.

VI. RESULTS AND DISCUSSION

The inversion algorithm converged to the solution in a few tens of iterations, which involved several hundreds of calls to the forward model (including the finite-difference approximation of the gradient at each iteration). This represents about 5 min of computation on a modest laptop computer [Intel core i5-4210 (Santa Clara, CA), 4 GB of random access memory (RAM)]. With our implementation of the semi-analytical method, the computation time with respect to the FEM analysis was about 3 orders of magnitude faster. Consequently, an inversion based on the FEM implementation would have taken several days to complete. Moreover, it should be noted that

because the shape of the inclusion was updated at each iteration, this would have caused difficulties with FEM due to the necessity to re-mesh the domain after each iteration. Even if the semi-analytical inverse problem implementation was faster than the FEM solution, the current time needed to obtain the viscoelasticity moduli at convergence may not be appropriate for clinical applications, but might be significantly decreased with the use of much faster programming language instead of MATLAB (MathWorks, Natick, MA), the parallelization of codes on central and graphic processing units, and the use of a more powerful computer.

Figure 7 compares pictures of the estimated inclusion geometries with B-mode images and elasticity maps

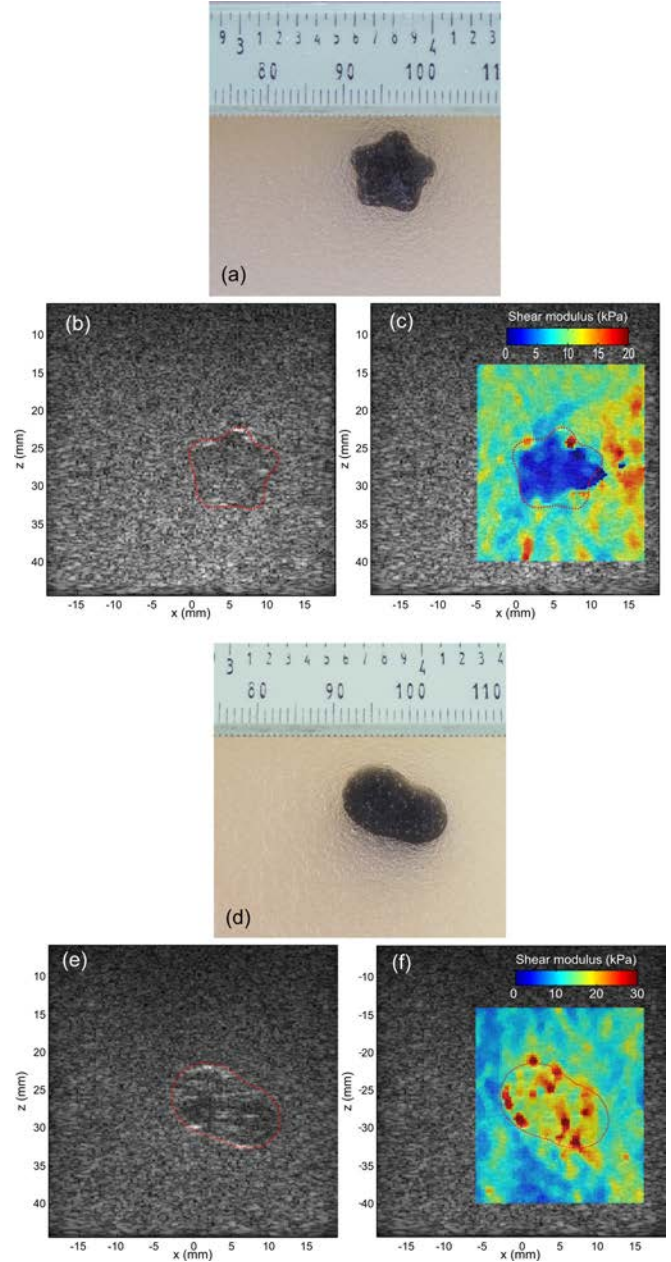


FIG. 7. (Color online) (a),(d) Photographs of the inclusions visible by the addition of graphite powders into the agar-gelatin gel; (b),(e) estimated shapes obtained by the solution of the inverse problem (red contours) on top of B-mode images; and (c),(f) elasticity maps obtained with the conventional TOF method, with the shapes from the inverse problem also reported for direct comparison.

obtained using the conventional TOF algorithm. The inclusion geometry and location estimated with the inverse problem solution are traced in red on B-mode images. It can be observed that estimated shapes match well with photographed geometries, even for the rather complex star shape. The contrast present on B-mode images was not used to help estimating inclusion geometries, as the inverse problem is based only on the recorded shear wave propagation movie. This demonstrates the ability of the proposed approach to localize and accurately reconstruct complex inclusion geometries with minimal *a priori* information. In comparison, the conventional TOF approach, while able to detect and localize both soft (star) and stiff (bean) inclusions, is not able to provide a clear representation of the actual geometry. Moreover, elasticity images contain artefacts, as discussed in the next paragraph.

As also depicted in Fig. 7 for the soft inclusion, the area of low elasticity is smaller than the actual inclusion, and there are areas of high elasticity in the surrounding medium, particularly on the right of the inclusion. For the hard inclusion, the area of high elasticity extends significantly outside the actual inclusion and the variance is high. Figure 8 displays stiffness images obtained with the TOF method in the reference homogeneous materials. It can be observed that these maps have less variance than the corresponding regions of the maps for the phantoms containing the inclusions, particularly inside the stiff inclusion and outside the soft inclusion. This indicates that the variance observed in

the maps for the phantoms containing the inclusions is linked to the presence of the inclusions. Indeed, the TOF method assumes plane wave propagation, which is no longer true in the presence of stiffness contrasts. It can be observed (see Figs. 11 and 12) that the wavefronts are significantly distorted by the inclusions, e.g., on the right of the soft inclusion or on the bottom right of the stiff inclusion. These regions correspond to overestimated stiffness on the maps of Fig. 7. A directional filter removing reflected waves,²⁴ as employed here, does not prevent these artefacts from appearing. However, repeating the experiment with pushes on both sides of the inclusion and combining the results would likely reduce the error.

The discrepancy between B-mode and elasticity images obtained with the TOF algorithm has been previously reported.⁴⁶ The proposed approach seems able to overcome this difficulty, although it would have to be tested *in vivo*. As described next, significant advantages over the TOF approach are the estimation of the loss modulus (viscosity) and the spectroscopic viscoelasticity analysis. However, a limitation is that binary viscoelasticity values are obtained inside and outside the inclusion (in other words, no viscoelasticity images are produced).

Figures 9 and 10 (soft star and hard bean) compare estimated viscoelastic properties, inside and outside the inclusion, to the results of the reference method. It should be remembered that these values are obtained from the estimated frequency dependent velocity $c(f)$ and constant

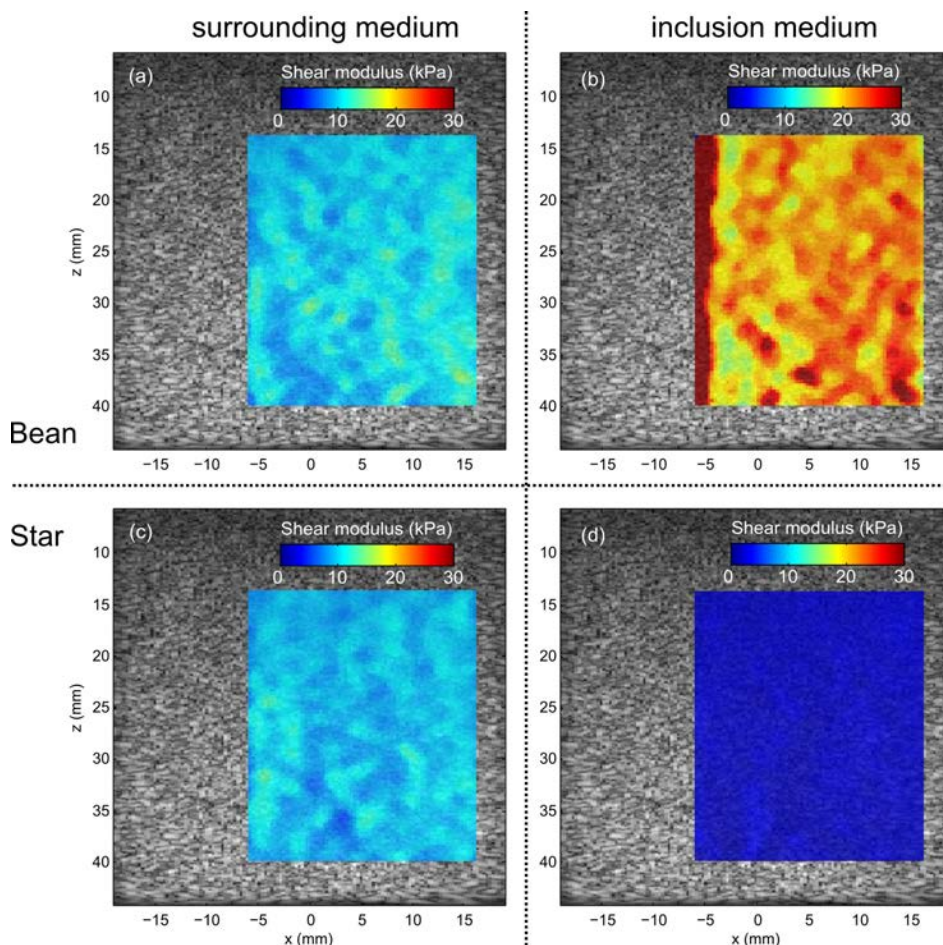


FIG. 8. (Color online) Elasticity maps obtained with the conventional TOF method in the homogeneous reference materials for the surrounding region and inclusions.

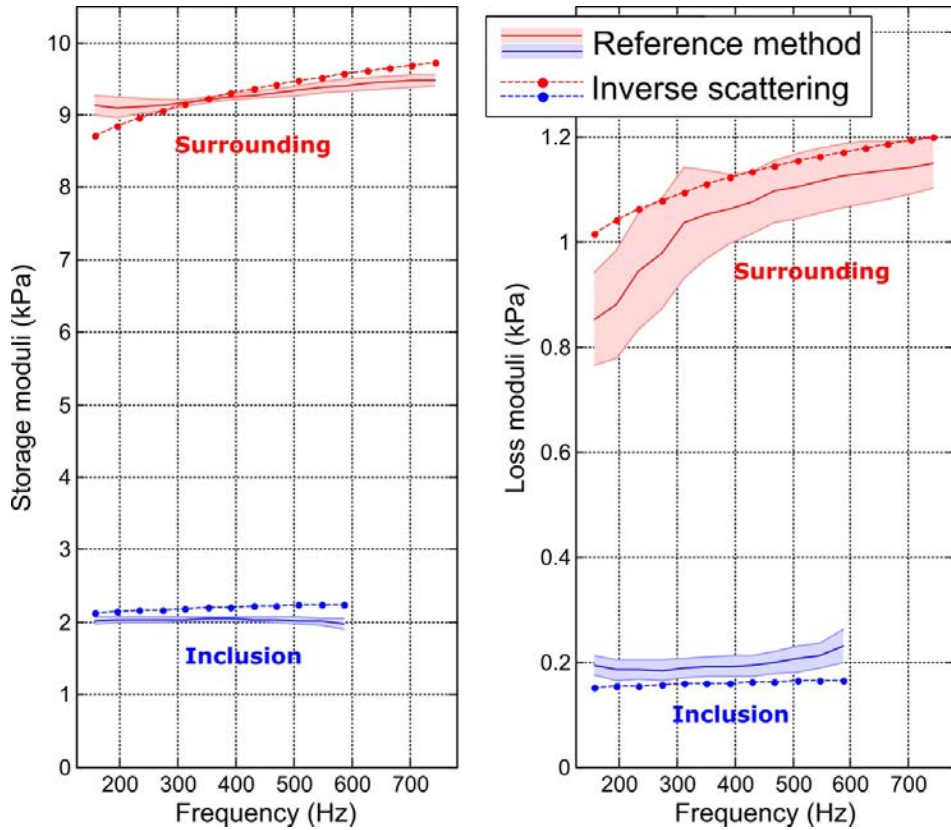


FIG. 9. (Color online) Estimated shear storage and loss moduli for the soft star-shaped inclusion and its surrounding medium, compared with the reference measurements in corresponding homogeneous materials. Note that the inverse scattering was solved for the wave velocity $c(\omega)$ and linear attenuation coefficient α_0 , from which the moduli were computed [Eqs. (26) and (27)].

attenuation coefficient α_0 through Eqs. (26) and (27). For the soft star phantom, the values of the attenuation coefficients were 0.1784 and 0.1287 Np/m/Hz for the inclusion and surrounding materials, respectively. For the stiff bean phantom,

these values were 0.0355 and 0.0853 Np/m/Hz for the inclusion and surrounding medium, respectively. For both phantoms, the storage and loss moduli estimated within the surrounding medium are in good agreement with values of

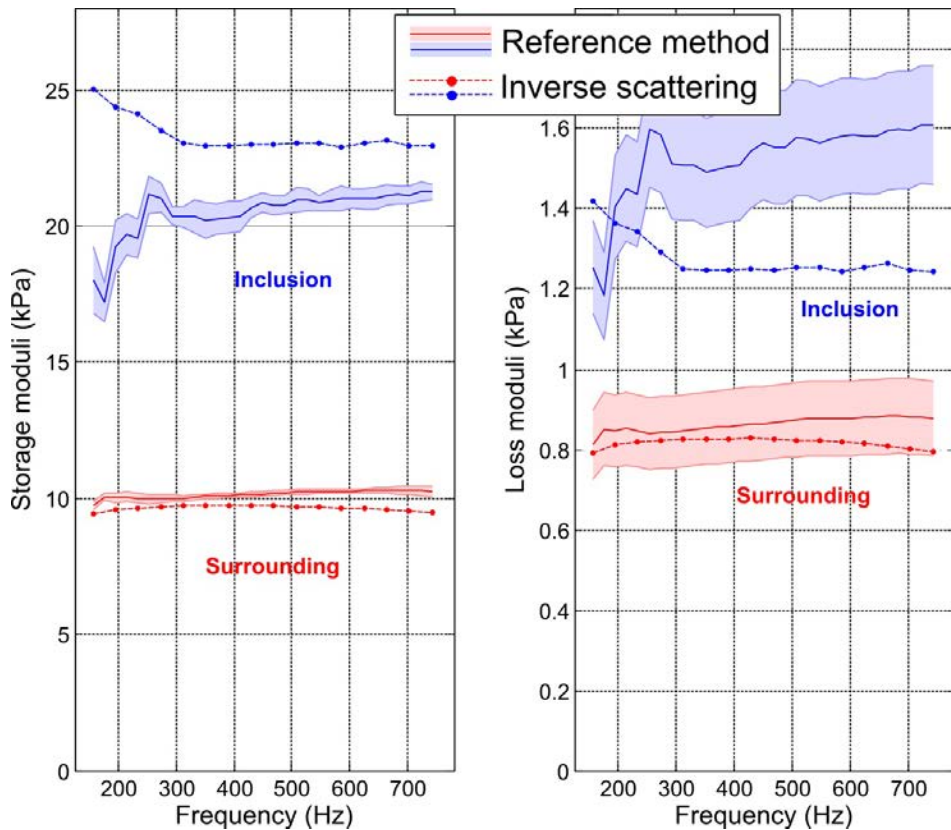


FIG. 10. (Color online) Estimated shear storage and loss moduli for the stiff bean-shaped inclusion and its surrounding medium, compared with the reference measurements in corresponding homogeneous materials. Note that the inverse scattering was solved for the wave velocity $c(\omega)$ and linear attenuation coefficient α_0 , from which the moduli were computed [Eqs. (26) and (27)].

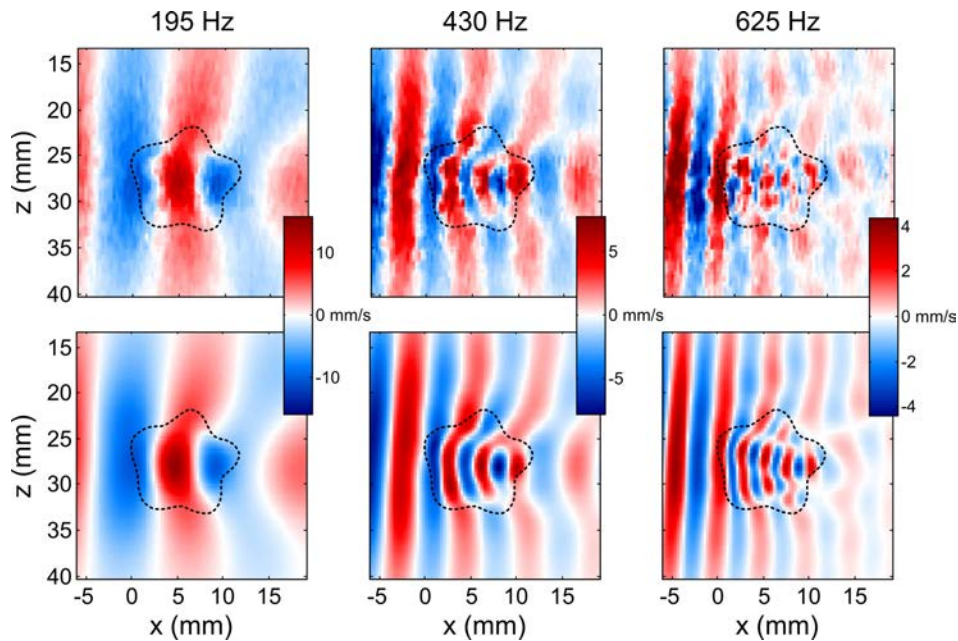


FIG. 11. (Color online) Experimental (top) and modeled (bottom) y -polarized wave fields for the soft star-shaped inclusion at low (195 Hz), mid (430 Hz), and high frequencies (625 Hz). The modeled fields are obtained for the optimized geometrical and mechanical parameters.

the reference method, over the whole frequency bandwidth: relative differences are $<8\%$ (average 3%) for the storage moduli and $<20\%$ (average 6%) for the loss moduli. In the case of the soft star-shaped inclusion, there is also a good agreement: errors $<14\%$ (average 8%) for the storage moduli and $<29\%$ (average 19%) for the loss moduli. In that case, we could not get accurate reference measurements for the inclusion properties above 600 Hz, due to a poor signal-to-noise ratio and the short wavelength (because of the low shear wave speed, see the next paragraph). Inside the hard bean-shaped inclusion, there is a larger discrepancy in the estimated storage moduli: the errors in the lowest frequencies reached 39%, but are $<14\%$ for frequencies over 300 Hz. A possible explanation for the larger errors at low frequencies is given in the next paragraph. For the loss moduli, the errors are $<23\%$ (average 17%). The elasticity

contrast is about 4.5 for the soft case and about 2.5 for the stiff inclusion, close to the contrast of 3 used in the numerical validation of the model.

Figures 11 and 12 compare experimental and modeled wave fields after convergence of the inverse problem to the best fitting parameters at low (195 Hz), mid (430 Hz), and high (625 Hz) frequencies. Experimental and modeled wave fields are comparable. All features, such as the change in wavelength inside the inclusion, deformation of the wavefront after the inclusion, attenuation, and interference patterns, are captured by the model. This constitutes an additional validation of the forward problem modeling. For the soft star at high frequency, it becomes more difficult to clearly distinguish the scattering pattern inside the inclusion. This is because the wavelength is close to the resolution of the imaging system and is very short (because of the high

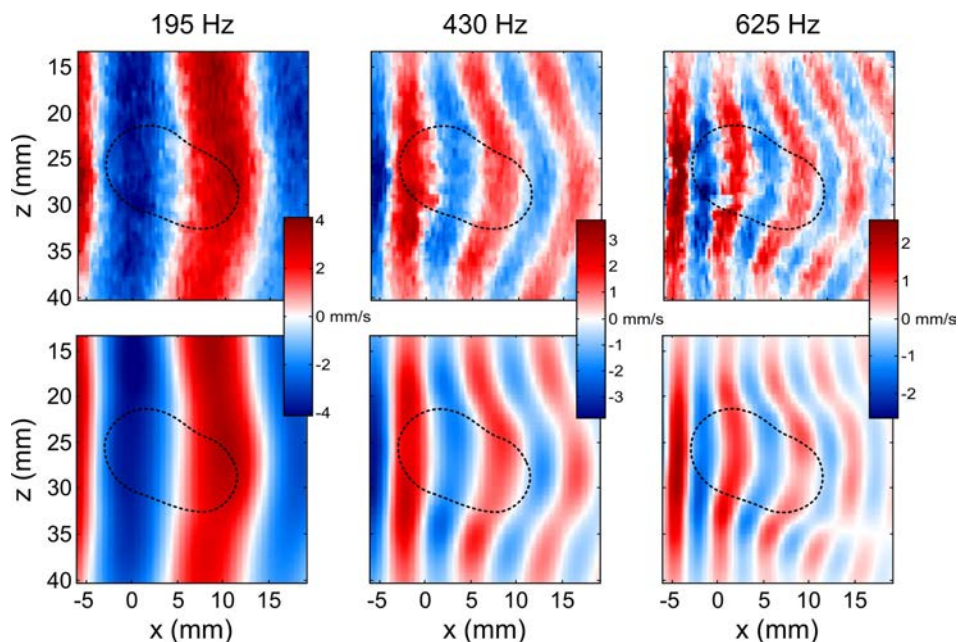


FIG. 12. (Color online) Experimental (top) and modeled (bottom) y -polarized wave fields for the stiff bean-shaped inclusion at low (195 Hz), mid (430 Hz), and high frequencies (625 Hz). The modeled fields are obtained for the optimized geometrical and mechanical parameters.

frequency and low shear wave speed). This set a high frequency limit for the estimation of the mechanical properties that is dependent on the shear wave speed. For the hard inclusion, we can see that there is about half a wavelength of propagation distance inside the inclusion at 195 Hz (Fig. 12). This may explain why the estimation of the inclusion storage modulus is not accurate in that case. Indeed, the storage modulus is primarily linked to the wave speed, and hence to the wavelength, which is difficult to precisely estimate over such a short propagation distance. This difficulty was already reported³⁵ and is related to the physics of the wave propagation and not to the inversion method.

Figure 13 shows experimental and modeled x -polarized fields (acquired by probe #2; see Fig. 6) for both inclusions at a frequency of 350 Hz. These experimental data were *not included* in the inverse problem, and therefore did not contribute to the parameter estimation. Nonetheless, the modeled fields match the complex experimental patterns of scattered waves. This comparison with independent data gives additional confidence in the estimated geometrical and mechanical parameters, and further validates the scattering model. These images also indicate that the wave field polarized in the direction orthogonal to the ultrasound beam axis contains information regarding the inclusion shape, location, and viscoelasticity. This is mostly because the x -polarized wave component is generated precisely at the inclusion boundary from mode conversion of the incident y -polarized wave. Adding these data in the inverse problem would surely improve the estimation of parameters. However, as already mentioned, this polarization cannot, as of today, be accurately measured from a single probe configuration in clinical elastography settings. An experimental system able to measure this component of the wave field, combined with a proper processing method, would potentially yield significant improvements to the field of SWE imaging.

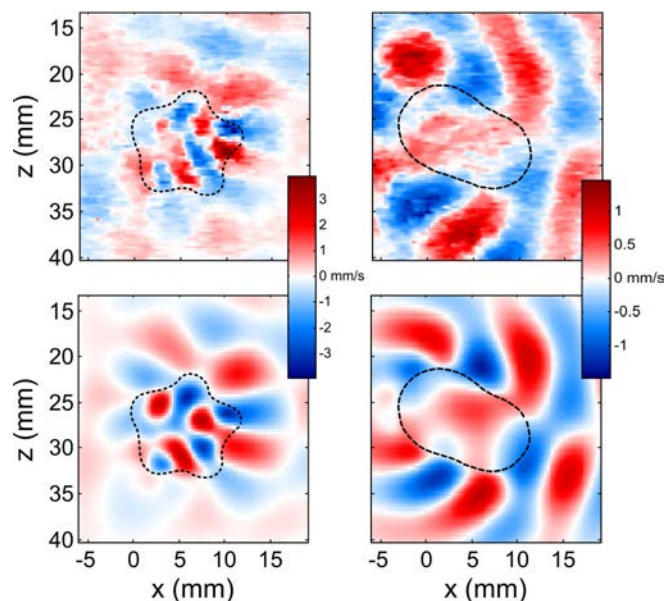


FIG. 13. (Color online) x -polarized wave fields for both inclusions at 350 Hz; the experimental fields (top) were not included in the inverse problem but still match well to the modeled fields (bottom).

The results presented so far were obtained for inversion performed with the maximum Fourier series order Q [Eq. (28)], which parametrizes the complexity of the shape, set to the expected value [i.e., $Q = 2$ for the bean shape and $Q = 5$ for the star shape, according to the definition of the shapes in Eqs. (24) and (25)]. However, this number would not be known *a priori* in real situations. The inversion was therefore performed again for the soft star inclusion with Q varying from 0 to 8 to evaluate the ability of the method to determine the correct order based on an analysis of the misfit residuals. The results are presented in Fig. 14. It can be observed that the norm of the residual decreases strongly for $Q = 4$ and $Q = 5$, but is almost constant for $Q > 5$. This indicates that, after $Q = 5$, providing more degrees-of-freedom to the inversion (i.e., allowing more complex shapes) does not significantly improve the fit to the experimental data, and that this number is therefore appropriate to accurately describe the shape of the inclusion.

The ROI was selected here so that the excitation does not vary considerably over the considered depth (see Figs. 11 and 12), and the pushing depths (25, 30, 35 mm) were selected according to the inclusion depth (about 30 mm). In that case, the signal-to-noise ratio was sufficient over a height of about 25 mm, from about 15 to 40 mm from the surface. Larger inclusions, or inclusions lying closer to the surface or deeper into the tissues, might require an adaption of the excitation procedure. This might be done by adding a fourth push, or by using an adapted beamforming strategy for an increased excitation height.⁴⁷

The loss moduli of the tested materials are relatively low compared to what can be observed for real tissues. This is a limitation of phantom studies, as it is difficult to reproduce the level of attenuation observed in tissues with agar and gelatin gels, even with the addition of oil.²⁹ Displacements would likely be noisier far from the pushing line in real tissues. However, it is important to consider that the present approach is not local, as global moduli are estimated for the surrounding medium and for the inclusions. Therefore, the

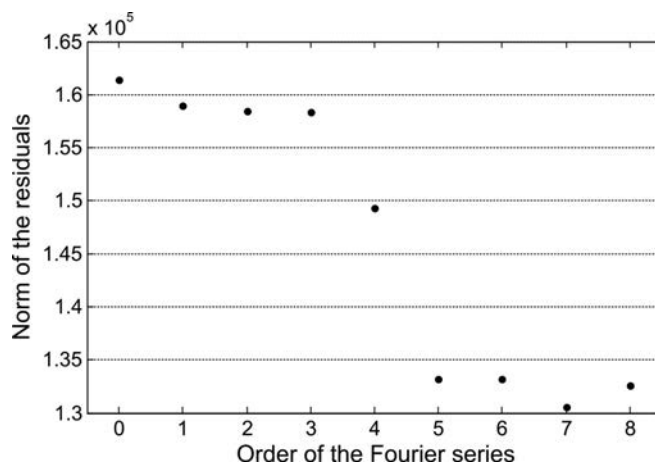


FIG. 14. Norm of the residuals at the end of the minimization problem for increasing order of the Fourier series describing the shape in the case of the soft-star inclusion. The expected order, from the definition of the shape [Eq. (25)], is $Q = 5$. It can be observed that, in practice, the misfit does not decrease anymore for $Q > 5$, indicating that the additional degrees-of-freedom are indeed not necessary to describe the shape.

displacements observed in the whole frame contribute to the estimations and the method can be expected to be less sensitive than local inversion to a decrease in signal-to-noise ratio far from the pushes. This should be tested on real tissues in future works.

VII. SUMMARY AND CONCLUSION

In this study, we first developed a semi-analytical model for the computation of elastic wave scattering by cylinders of irregular cross section. This work is an extension of the contribution of Léon *et al.*³⁹ on acoustic scattering by such cylinders. The elastic case developed in the current study is more complicated, due to the vectorial nature of the displacement field, opposed to the acoustic scalar pressure field. For the sake of simplicity, we have considered a normal incidence on the cylinder. In that case, the problem decouples into two separate smaller problems: one for SH waves, and one for SV and longitudinal (compression) waves. The general case of an oblique incidence could, however, be considered by the same approach.

The computation method was validated in the case of soft viscoelastic solids against 2D FEM for two irregular cross sections, a bean shape, and a more complex five branches star. Good agreement was observed between both methods at kR numbers of 5. At higher frequencies, numerical problems arose in the semi-analytical approach, mostly due to the need of higher orders Bessel and Hankel functions, which have a very large dynamic range that can rapidly exceed the computer double precision, as illustrated by the shifted circular cylinder example. This method is therefore not able to compute scattering at high frequencies. Numerical approaches such as finite differences or finite elements may be more appropriate in that case. Although it was validated in the context of soft solids, the approach is general and could be applied as well for hard solids in other domains in which elastic waves are used for material characterization such as non-destructive testing or seismology. Other applications would, however, require performing an analysis of the optimal truncation numbers N and M as done here.

In the second part of this study, we experimentally measured the scattered field for a shear wave incident on irregular cylinders with different elasticity contrast (soft star and stiff bean, as considered in the numerical validation). The shear wave was generated using an acoustic radiation force mimicking SSI. We then used the scattering field in an inverse problem approach to jointly estimate the shape, position, and viscoelasticity of the inclusions in the imaging plane. After convergence of the parameters, we observed good agreement between computed and measured wave fields over the whole frequency bandwidth of the elastography method. Notably, the field polarized in the x -direction, which was not included in the inverse problem but used only for *a posteriori* validation, also showed good agreement. The parameters estimated by this approach were compared to parameters measured on corresponding homogenous materials and were found to agree. This experimental part, therefore, validated the scattering model and demonstrated its potential for material characterization.

The mechanical parameters estimated with the inverse scattering method agreed within $\sim 10\%$ for the storage modulus (except for very low frequencies in the stiff inclusion), and $\sim 20\%$ – 30% for the loss modulus, with reference measurements obtained from other elastography methods on homogeneous materials. Similar accuracies were observed in previous applications of similar approaches with quasi plane shear waves^{34,35} or torsional shear waves,³¹ the latter method originally proposed by Hadj-Henni *et al.*⁴⁸ However, a significant improvement over these previous studies is that the location and shape of the inclusions were not known *a priori* here, but estimated along with the mechanical parameters. Moreover, the estimated shapes of the inclusions were in good visual agreement with the photography and B-mode images of the phantoms. This may allow, in the future, accurate estimation of geometrical parameters of soft tissue lesions, for example, in the context of breast cancer screening and treatment monitoring. In this context, the stiff bean-shaped inclusion is a more relevant example than the star-shaped soft inclusions, as most breast lesions, either benign or malignant, are usually stiffer than the surrounding tissues.⁴⁶ However, the soft-star inclusion helps to demonstrate the generality of the approach.

We have realized important steps for estimating viscoelastic properties, shape, and position of soft tissue inclusions. However, difficulties remain to be addressed for *in vivo* applications in the context of breast cancer diagnostic: (1) real inclusions are 3D, and are not infinitely long in one dimension. Therefore, a 3D scattering model might be necessary. It is questionable, however, if the present 2D approach would still be successful for 3D applications. This could be investigated in future works. (2) In real cases, the inclusion and the surrounding medium would not be homogenous, as is the case here. The present method is, by construction, limited to piecewise homogeneous materials separated by a closed boundary, and cannot be easily modified to handle more complex media. It is therefore necessary to test the method under more challenging situations like, for example, viscoelasticity modulus gradient in the inclusion and surrounding medium, or a smooth transition between both media. It would be important to determine in which conditions the method can continue to provide good estimates of the mechanical and geometrical properties.

To conclude, the present results demonstrated that it is possible to extract more information from shear wave propagation movies than it is extracted with the usual TOF method in a setup close to clinical settings and using an efficient semi-analytical model of wave scattering by irregular inclusions.

ACKNOWLEDGMENT

S.B. was supported by a MÉDITIS postdoctoral fellowship of the Natural Sciences and Engineering Research Council of Canada provided by the Institute of Biomedical Engineering of the École Polytechnique and University of Montréal. This work was supported by the Fonds de Recherche du Québec–Nature et Technologies under Grant No. PR-174387. The authors are grateful to Boris Chayer for help with the 3D printer.

APPENDIX A: DISPLACEMENT AND STRAIN EXPRESSIONS

From the Helmholtz decomposition (2) we can get the expressions of the displacement and strain field components

$$u_j^r = \frac{\partial \varphi_j}{\partial r} + \frac{1}{r} \frac{\partial \psi_i}{\partial \theta}, \quad (\text{A1})$$

$$u_j^\theta = \frac{1}{r} \frac{\partial \varphi_j}{\partial \theta} - \frac{\partial \psi_i}{\partial r}, \quad (\text{A2})$$

$$u_j^z = \frac{a}{r} \left(-r \frac{\partial^2 \chi_j}{\partial r^2} - \frac{\partial \chi_j}{\partial r} - \frac{1}{r} \frac{\partial^2 \chi_j}{\partial \theta^2} \right), \quad (\text{A3})$$

$$\varepsilon_j^{rr} = \frac{\partial^2 \varphi_j}{\partial r^2} + \frac{1}{r} \frac{\partial^2 \psi_i}{\partial \theta \partial r} - \frac{1}{r^2} \frac{\partial \psi_i}{\partial \theta}, \quad (\text{A4})$$

$$\varepsilon_j^{\theta\theta} = \frac{1}{r^2} \frac{\partial^2 \varphi_j}{\partial \theta^2} + \frac{1}{r} \frac{\partial \varphi_j}{\partial r} - \frac{1}{r} \left(\frac{\partial^2 \psi_i}{\partial \theta \partial r} - \frac{1}{r} \frac{\partial \psi_i}{\partial \theta} \right), \quad (\text{A5})$$

$$\varepsilon_j^{zz} = 0, \quad (\text{A6})$$

$$\varepsilon_j^{\theta z} = \frac{a}{2} \left(-\frac{1}{r} \frac{\partial^3 \chi_j}{\partial \theta \partial r^2} - \frac{1}{r^3} \frac{\partial^3 \chi_j}{\partial \theta^3} - \frac{1}{r^2} \frac{\partial^2 \chi_j}{\partial \theta \partial r} \right), \quad (\text{A7})$$

$$\varepsilon_j^{rz} = \frac{a}{2} \left(-\frac{\partial^3 \chi_j}{\partial r^3} - \frac{1}{r} \frac{\partial^2 \chi_j}{\partial r^2} - \frac{1}{r^2} \frac{\partial^3 \chi_j}{\partial \theta^2 \partial r} + \frac{1}{r^3} \frac{\partial^2 \chi_j}{\partial \theta^2} + \frac{1}{r^2} \frac{\partial \chi_j}{\partial r} \right), \quad (\text{A8})$$

$$\varepsilon_j^{r\theta} = \frac{1}{2} \left[\frac{2}{r} \frac{\partial^2 \varphi_j}{\partial r \partial \theta} - \frac{2}{r^2} \frac{\partial \varphi_j}{\partial \theta} + \frac{1}{r^2} \left(\frac{\partial^2 \psi_i}{\partial \theta^2} - r^2 \frac{\partial^2 \psi_i}{\partial r^2} + r \frac{\partial \psi_i}{\partial r} \right) \right]. \quad (\text{A9})$$

The stresses are obtained from the Hooke's law for isotropic media

$$\begin{aligned} \sigma_j^{rr} &= (\lambda_j + 2\mu_j) \frac{\partial^2 \varphi_j}{\partial r^2} + \lambda_j \left(\frac{1}{r^2} \frac{\partial^2 \varphi_j}{\partial \theta^2} + \frac{1}{r} \frac{\partial \varphi_j}{\partial r} \right) \\ &\quad + 2\mu_j \left(\frac{1}{r} \frac{\partial^2 \psi_i}{\partial \theta \partial r} - \frac{1}{r^2} \frac{\partial \psi_i}{\partial \theta} \right), \end{aligned} \quad (\text{A10})$$

$$\begin{aligned} \sigma_j^{\theta\theta} &= (\lambda_j + 2\mu_j) \left(\frac{1}{r^2} \frac{\partial^2 \varphi_j}{\partial \theta^2} + \frac{1}{r} \frac{\partial \varphi_j}{\partial r} \right) + \lambda_j \frac{\partial^2 \varphi_j}{\partial r^2} \\ &\quad + 2\mu_j \left(\frac{1}{r^2} \frac{\partial \psi_i}{\partial \theta} - \frac{1}{r} \frac{\partial^2 \psi_i}{\partial \theta \partial r} \right), \end{aligned} \quad (\text{A11})$$

$$\sigma_j^{zz} = \lambda_j \left(\frac{\partial^2 \varphi_j}{\partial r^2} + \frac{1}{r^2} \frac{\partial^2 \varphi_j}{\partial \theta^2} + \frac{1}{r} \frac{\partial \varphi_j}{\partial r} \right), \quad (\text{A12})$$

$$\sigma_j^{\theta z} = \mu_j a \left(-\frac{1}{r} \frac{\partial^3 \chi_j}{\partial \theta \partial r^2} - \frac{1}{r^3} \frac{\partial^3 \chi_j}{\partial \theta^3} - \frac{1}{r^2} \frac{\partial^2 \chi_j}{\partial \theta \partial r} \right), \quad (\text{A13})$$

$$\sigma_j^{rz} = \mu_j a \left(-\frac{\partial^3 \chi_j}{\partial r^3} - \frac{1}{r} \frac{\partial^2 \chi_j}{\partial r^2} - \frac{1}{r^2} \frac{\partial^3 \chi_j}{\partial \theta^2 \partial r} + \frac{1}{r^3} \frac{\partial^2 \chi_j}{\partial \theta^2} + \frac{1}{r^2} \frac{\partial \chi_j}{\partial r} \right), \quad (\text{A14})$$

$$\sigma_j^{r\theta} = \mu_j \left[\frac{2}{r} \frac{\partial^2 \varphi_j}{\partial r \partial \theta} - \frac{2}{r^2} \frac{\partial \varphi_j}{\partial \theta} + \frac{1}{r^2} \left(\frac{\partial^2 \psi_i}{\partial \theta^2} - r^2 \frac{\partial^2 \psi_i}{\partial r^2} + r \frac{\partial \psi_i}{\partial r} \right) \right]. \quad (\text{A15})$$

APPENDIX B: BESSEL AND HANKEL DECOMPOSITIONS

To simplify the expressions for the mechanical fields obtained when inserting the Bessel decompositions Eqs. (5)–(10) in Eqs. (A1)–(A15), we introduce the following notation for the derivatives of the Bessel functions, where the superscript L stands for longitudinal (compression) waves and T means transverse (shear) waves:

$$a_n^{L,1}(r) = J_n(K_1 r), \quad (\text{B1})$$

$$b_n^{L,1}(r) = \frac{1}{2} K_1 [J_{n-1}(K_1 r) - J_{n+1}(K_1 r)], \quad (\text{B2})$$

$$c_n^{L,1}(r) = \frac{1}{4} K_1^2 [J_{n-2}(K_1 r) - 2J_n(K_1 r) + J_{n+2}(K_1 r)], \quad (\text{B3})$$

$$a_n^{T,1}(r) = J_n(k_1 r), \quad (\text{B4})$$

$$b_n^{T,1}(r) = \frac{1}{2} k_1 [J_{n-1}(k_1 r) - J_{n+1}(k_1 r)], \quad (\text{B5})$$

$$c_n^{T,1}(r) = \frac{1}{4} k_1^2 [J_{n-2}(k_1 r) - 2J_n(k_1 r) + J_{n+2}(k_1 r)], \quad (\text{B6})$$

$$\begin{aligned} d_n^{T,1}(r) &= \frac{1}{8} k_1^3 [J_{n-3}(k_1 r) - 3J_{n-1}(k_1 r) \\ &\quad + 3J_{n+1}(k_1 r) - J_{n+3}(k_1 r)], \end{aligned} \quad (\text{B7})$$

$$a_n^{L,2}(r) = H_n^1(K_2 r), \quad (\text{B8})$$

$$b_n^{L,2}(r) = \frac{1}{2} K_2 [H_{n-1}^1(K_2 r) - H_{n+1}^1(K_2 r)], \quad (\text{B9})$$

$$c_n^{L,2}(r) = \frac{1}{4} K_2^2 [H_{n-2}^1(K_2 r) - 2H_n^1(K_2 r) + H_{n+2}^1(K_2 r)], \quad (\text{B10})$$

$$a_n^{T,2}(r) = H_n^1(k_2 r), \quad (\text{B11})$$

$$b_n^{T,2}(r) = \frac{1}{2} k_2 [H_{n-1}^1(k_2 r) - H_{n+1}^1(k_2 r)], \quad (\text{B12})$$

$$c_n^{T,2}(r) = \frac{1}{4} k_2^2 [H_{n-2}^1(k_2 r) - 2H_n^1(k_2 r) + H_{n+2}^1(k_2 r)], \quad (\text{B13})$$

and

$$\begin{aligned} d_n^{T,2}(r) &= \frac{1}{8} k_2^3 [H_{n-3}^1(k_2 r) - 3H_{n-1}^1(k_2 r) \\ &\quad + 3H_{n+1}^1(k_2 r) - H_{n+3}^1(k_2 r)]. \end{aligned} \quad (\text{B14})$$

The displacement and stress field components are, then, for medium 1,

$$u_1^r(r, \theta) = \sum_{n=-\infty}^{+\infty} \left(A_n b_n^{L,1}(r) + \frac{in}{r} B_n a_n^{T,1}(r) \right) e^{in\theta}, \quad (\text{B15})$$

$$u_1^\theta(r, \theta) = \sum_{n=-\infty}^{+\infty} \left(\frac{in}{r} A_n a_n^{L,1}(r) - B_n b_n^{T,1}(r) \right) e^{in\theta}, \quad (\text{B16})$$

$$u_1^z(r, \theta) = \sum_{n=-\infty}^{+\infty} \left[\frac{a}{r} C_n \left(-b_n^{T,1}(r) - r c_n^{T,1} + \frac{n^2}{r} a_n^{T,1}(r) \right) \right] e^{in\theta}, \quad (\text{B17})$$

$$\sigma_1^r(r, \theta) = \sum_{n=-\infty}^{+\infty} \left\{ A_n \left[(\lambda_1 + 2\mu_1) c_n^{L,1}(r) - \lambda_1 \left(\frac{n^2}{r^2} a_n^{L,1}(r) - \frac{1}{r} b_n^{L,1}(r) \right) \right] + 2\mu_1 B_n \frac{in}{r} \left(b_n^{T,1}(r) - \frac{a_n^{T,1}(r)}{r} \right) \right\} e^{in\theta}, \quad (\text{B18})$$

$$\sigma_1^{\theta\theta}(r, \theta) = \sum_{n=-\infty}^{+\infty} \left\{ A_n \left[(\lambda_1 + 2\mu_1) \left(-\frac{n^2}{r^2} a_n^{L,1}(r) + \frac{b_n^{L,1}(r)}{r} \right) + \lambda_1 c_n^{L,1}(r) \right] + B_n 2\mu_1 \frac{in}{r} \left(\frac{a_n^{T,1}(r)}{r} - b_n^{T,1}(r) \right) \right\} e^{in\theta}, \quad (\text{B19})$$

$$\sigma_1^{zz}(r, \theta) = \sum_{n=-\infty}^{+\infty} A_n \lambda_1 \left(c_n^{L,1}(r) - \frac{n^2}{r^2} a_n^{L,1}(r) + \frac{b_n^{L,1}(r)}{r} \right) e^{in\theta}, \quad (\text{B20})$$

$$\sigma_1^{\theta z}(r, \theta) = \sum_{n=-\infty}^{+\infty} \mu_1 a C_n \left[-\frac{in}{r} c_n^{T,1} - \frac{in}{r^2} c_n^{T,1} + a_n^{T,1} \left(\frac{in^3}{r^3} \right) \right] e^{in\theta}, \quad (\text{B21})$$

$$\sigma_1^{rz}(r, \theta) = \sum_{n=-\infty}^{+\infty} \mu_1 a C_n \left[b_n^{T,1} \left(\frac{1}{r^2} + \frac{n^2}{r^2} \right) - d_n^{T,1} - \frac{c_n^{T,1}}{r} - \frac{n^2}{r^3} a_n^{T,1} \right] e^{in\theta}, \quad (\text{B22})$$

and

$$\sigma_1^{\theta r}(r, \theta) = \sum_{n=-\infty}^{+\infty} \left[A_n 2\mu_1 \frac{in}{r} \left(b_n^{L,1}(r) - \frac{1}{r} a_n^{L,1}(r) \right) + \frac{B_n}{r^2} \mu_1 \left(-n^2 a_n^{T,1}(r) - r^2 c_n^{T,1}(r) + r b_n^{T,1}(r) \right) \right] e^{in\theta}. \quad (\text{B23})$$

Expressions for medium 2 can be easily obtained by changing the sub- and superscripts and replacing A_n , B_n , and C_n with D_n , E_n , and F_n , respectively.

APPENDIX C: FOURIER COEFFICIENTS

To remove the dependence on the angular variable θ in the boundary conditions, the Fourier series coefficients u_q^k and σ_q^k are defined for the incident fields

$$u_{\text{inc}}^k(\theta) = \sum_{q=-\infty}^{+\infty} u_q^k e^{iq\theta} \quad \text{for } k = r, \theta, \text{ or } z \quad (\text{C1})$$

and

$$(\sigma_{\text{inc}}^{kr} n_r + \sigma_{\text{inc}}^{k\theta} n_\theta)(\theta) = \sum_{q=-\infty}^{+\infty} \sigma_q^k e^{iq\theta} \quad \text{for } k = r, \theta, \text{ or } z, \quad (\text{C2})$$

and $\alpha_{n,q}^{\tau,j}$, $\beta_{n,q}^{\tau,j}$, $\gamma_{n,q}^{T,j}$, $\delta_{n,q}^j$, $\epsilon_{n,q}^j$, $\zeta_{n,q}^j$, $\eta_{n,q}^j$, and $\kappa_{n,q}^j$ for the refracted and diffracted fields

$$\frac{in}{R(\theta)} a_n^{\tau,j}(\theta) = \sum_{q=-\infty}^{+\infty} \alpha_{n,q}^{\tau,j} e^{iq\theta} \quad \text{for } \tau = (L, T) \text{ and } j = (1, 2), \quad (\text{C3})$$

$$b_n^{\tau,j}(\theta) = \sum_{q=-\infty}^{+\infty} \beta_{n,q}^{\tau,j} e^{iq\theta} \quad \text{for } \tau = (L, T) \text{ and } j = (1, 2), \quad (\text{C4})$$

$$\frac{a}{r} \left(-b_n^{T,j}(\theta) - r c_n^{T,j}(\theta) + \frac{n^2}{r} a_n^{T,j}(\theta) \right) = \sum_{q=-\infty}^{+\infty} \gamma_{n,q}^{T,j} e^{iq\theta} \quad \text{for } j = (1, 2), \quad (\text{C5})$$

$$\begin{aligned} & \left[(\lambda_j + 2\mu_j) c_n^{L,j}(\theta) - \lambda_j \left(\frac{n^2}{R(\theta)^2} a_n^{L,j}(\theta) - \frac{1}{R(\theta)} b_n^{L,j}(\theta) \right) \right] n_r + 2\mu_j \frac{in}{R(\theta)} \left(b_n^{L,j}(\theta) - \frac{1}{R(\theta)} a_n^{L,j}(\theta) \right) n_\theta \\ & = \sum_{q=-\infty}^{+\infty} \delta_{n,q}^j e^{iq\theta} \quad \text{for } j = (1, 2), \end{aligned} \quad (\text{C6})$$

$$2\mu_j \frac{in}{R(\theta)} \left(b_n^{Tj}(\theta) - \frac{a_n^{Tj}(\theta)}{R(\theta)} \right) n_r + \frac{\mu_j}{R(\theta)^2} \left(-n^2 a_n^{Tj}(\theta) - R(\theta)^2 c_n^{Tj}(\theta) + r b_n^{Tj}(\theta) \right) n_\theta = \sum_{q=-\infty}^{+\infty} \xi_{n,q}^j e^{iq\theta} \quad \text{for } j = (1, 2), \quad (C7)$$

$$2\mu_j \frac{in}{R(\theta)} \left(b_n^{Lj}(\theta) - \frac{1}{R(\theta)} a_n^{Lj}(\theta) \right) n_r + \left[(\lambda_j + 2\mu_j) \left(-\frac{n^2}{R(\theta)^2} a_n^{Lj}(\theta) + \frac{b_n^{Lj}(\theta)}{R(\theta)} \right) + \lambda_1 c_n^{Lj}(\theta) \right] n_\theta = \sum_{q=-\infty}^{+\infty} \zeta_{n,q}^j e^{iq\theta} \quad \text{for } j = (1, 2), \quad (C8)$$

$$\frac{\mu_j}{R(\theta)^2} \left(-n^2 a_n^{Tj}(\theta) - r^2 c_n^{Tj}(\theta) + r b_n^{Tj}(\theta) \right) n_r + 2\mu_j \frac{in}{R(\theta)} \left(\frac{a_n^{Tj}(\theta)}{R(\theta)} - b_n^{Tj}(\theta) \right) n_\theta = \sum_{q=-\infty}^{+\infty} \eta_{n,q}^j e^{iq\theta} \quad \text{for } j = (1, 2), \quad (C9)$$

and

$$\begin{aligned} & \mu_j \left[b_n^{Tj} \left(\frac{1}{R(\theta)^2} + \frac{n^2}{R(\theta)^2} \right) - a_n^{Tj} - \frac{c_n^{Tj}}{R(\theta)} - \frac{n^2}{R(\theta)^3} a_n^{Tj} \right] n_r + \mu_j \left[-\frac{in}{R(\theta)} c_n^{Tj} - \frac{in}{R(\theta)^2} c_n^{Tj} + a_n^{Tj} \left(\frac{in^3}{R(\theta)^3} \right) \right] n_\theta \\ & = \sum_{q=-\infty}^{+\infty} \kappa_{n,q}^j e^{iq\theta} \quad \text{for } j = (1, 2). \end{aligned} \quad (C10)$$

- ¹J. Ophir, I. Cespedes, H. Ponnekanti, Y. Yazdi, and X. Li, "Elastography: A quantitative method for imaging the elasticity of biological tissues," *Ultrason. Imaging* **13**(2), 111–134 (1991).
- ²A. Sarvazyan, T. J. Hall, M. W. Urban, M. Fatemi, S. R. Aglyamov, and B. S. Garra, "An overview of elastography—An emerging branch of medical imaging," *Curr. Med. Imaging Rev.* **7**(4), 255–282 (2011).
- ³K. R. Nightingale, M. L. Palmeri, R. W. Nightingale, and G. E. Trahey, "On the feasibility of remote palpation using acoustic radiation force," *J. Acoust. Soc. Am.* **110**(1), 625–634 (2001).
- ⁴L. Sandrin, M. Tanter, S. Catheline, and M. Fink, "Shear modulus imaging with 2-D transient elastography," *IEEE Trans. Ultrason. Ferroelectr. Freq. Control* **49**(4), 426–435 (2002).
- ⁵A. Manduca, T. E. Oliphant, M. Dresner, J. Mahowald, S. A. Kruse, E. Amromin, J. P. Felmlee, J. F. Greenleaf, and R. L. Ehman, "Magnetic resonance elastography: Non-invasive mapping of tissue elasticity," *Med. Image Anal.* **5**(4), 237–254 (2001).
- ⁶J. M. Schmitt, "OCT elastography: Imaging microscopic deformation and strain of tissue," *Opt. Express* **3**(6), 199–211 (1998).
- ⁷Y. Yamakoshi, J. Sato, and T. Sato, "Ultrasonic imaging of internal vibration of soft tissue under forced vibration," *IEEE Trans. Ultrason. Ferroelectr. Freq. Control* **37**(2), 45–53 (1990).
- ⁸A. P. Sarvazyan, O. V. Rudenko, S. D. Swanson, J. B. Fowlkes, and S. Y. Emelianov, "Shear wave elasticity imaging: A new ultrasonic technology of medical diagnostics," *Ultrason. Med. Biol.* **24**(9), 1419–1435 (1998).
- ⁹M. Fatemi and J. F. Greenleaf, "Ultrasound-stimulated vibro-acoustic spectrography," *Science* **280**(5360), 82–85 (1998).
- ¹⁰J. Bercoff, M. Tanter, and M. Fink, "Supersonic shear imaging: A new technique for soft tissue elasticity mapping," *IEEE Trans. Ultrason. Ferroelectr. Freq. Control* **51**(4), 396–409 (2004).
- ¹¹P. Grasland-Mongrain, E. Miller-Jolicoeur, A. Tang, S. Catheline, and G. Cloutier, "Contactless remote induction of shear waves in soft tissues using a transcranial magnetic stimulation device," *Phys. Med. Biol.* **61**(6), 2582–2593 (2016).
- ¹²P. Grasland-Mongrain, Y. Lu, F. Lesage, S. Catheline, and G. Cloutier, "Generation of shear waves by laser in soft media in the ablative and thermoelastic regimes," *Appl. Phys. Lett.* **109**(22), 221901 (2016).
- ¹³K. Nightingale, S. McAleavey, and G. Trahey, "Shear-wave generation using acoustic radiation force: *In vivo* and *ex vivo* results," *Ultrason. Med. Biol.* **29**(12), 1715–1723 (2003).
- ¹⁴S. Catheline, J. L. Gennisson, G. Delon, M. Fink, R. Sinkus, S. Abouelkaram, and J. Culioli, "Measurement of viscoelastic properties of homogeneous soft solid using transient elastography: An inverse problem approach," *J. Acoust. Soc. Am.* **116**(6), 3734–3741 (2004).
- ¹⁵K. Lin and J. McLaughlin, "An error estimate on the direct inversion model in shear stiffness imaging," *Inv. Problems* **25**(7), 075003 (2009).
- ¹⁶M. Tanter, J. Bercoff, A. Athanasiou, T. Deffieux, J. L. Gennisson, G. Montaldo, M. Muller, A. Tardivon, and M. Fink, "Quantitative assessment of breast lesion viscoelasticity: Initial clinical results using supersonic shear imaging," *Ultrason. Med. Biol.* **34**(9), 1373–1386 (2008).
- ¹⁷J. McLaughlin and D. Renzi, "Using level set based inversion of arrival times to recover shear wave speed in transient elastography and supersonic imaging," *Inv. Problems* **22**(2), 707–725 (2006).
- ¹⁸J. McLaughlin and D. Renzi, "Shear wave speed recovery in transient elastography and supersonic imaging using propagating fronts," *Inv. Problems* **22**(2), 681–706 (2006).
- ¹⁹N. C. Rouze, M. H. Wang, M. L. Palmeri, and K. R. Nightingale, "Parameters affecting the resolution and accuracy of 2-D quantitative shear wave images," *IEEE Trans. Ultrason. Ferroelectr. Freq. Control* **59**(8), 1729–1740 (2012).
- ²⁰R. S. Lakes, *Viscoelastic Materials* (Cambridge University Press, Cambridge, New York, 2009), pp. 1–457.
- ²¹Z. J. Domire, M. B. McCullough, Q. Chen, and K. N. An, "Wave attenuation as a measure of muscle quality as measured by magnetic resonance elastography: Initial results," *J. Biomech.* **42**(4), 537–540 (2009).
- ²²P. Garteiser, S. Doblas, J. L. Daire, M. Wagner, H. Leitao, V. Vilgrain, R. Sinkus, and B. E. Van Beers, "MR elastography of liver tumours: Value of viscoelastic properties for tumour characterization," *Eur. Radiol.* **22**(10), 2169–2177 (2012).
- ²³I. Z. Nenadic, B. Qiang, M. W. Urban, H. Zhao, W. Sanchez, J. F. Greenleaf, and S. Chen, "Attenuation measuring ultrasound shearwave elastography and *in vivo* application in post-transplant liver patients," *Phys. Med. Biol.* **62**(2), 484–500 (2016).
- ²⁴T. Deffieux, J. L. Gennisson, J. Bercoff, and M. Tanter, "On the effects of reflected waves in transient shear wave elastography," *IEEE Trans. Ultrason. Ferroelectr. Freq. Control* **58**(10), 2032–2035 (2011).
- ²⁵S. Chen, M. Fatemi, and J. F. Greenleaf, "Quantifying elasticity and viscosity from measurement of shear wave speed dispersion," *J. Acoust. Soc. Am.* **115**(6), 2781–2785 (2004).
- ²⁶T. Deffieux, G. Montaldo, M. Tanter, and M. Fink, "Shear wave spectroscopy for *in vivo* quantification of human soft tissues visco-elasticity," *IEEE Trans. Med. Imaging* **28**(3), 313–322 (2009).
- ²⁷S. Kazemirad, S. Bernard, S. Hybois, A. Tang, and G. Cloutier, "Ultrasound shear wave viscoelastography: Model-independent quantification of the complex shear modulus," *IEEE Trans. Ultrason. Ferroelectr. Freq. Control* **63**(9), 1399–1408 (2016).
- ²⁸E. Budelli, J. Brum, M. Bernal, T. Deffieux, M. Tanter, P. Lema, C. Negreira, and J. L. Gennisson, "A diffraction correction for storage and loss moduli imaging using radiation force based elastography," *Phys. Med. Biol.* **62**(1), 91–106 (2016).

- ²⁹S. Bernard, S. Kazemirad, and G. Cloutier, "A frequency-shift method to measure shear-wave attenuation in soft tissues," *IEEE Trans. Ultrason. Ferroelectr. Freq. Control* **64**(3), 514–524 (2017).
- ³⁰A. Hadj-Henni, C. Schmitt, and G. Cloutier, "Shear wave induced resonance elastography of soft heterogeneous media," *J. Biomech.* **43**(8), 1488–1493 (2010).
- ³¹A. Hadj-Henni, C. Schmitt, M. É. Tremblay, M. Hamdine, M. C. Heuzey, P. Carreau, and G. Cloutier, "Hyper-frequency viscoelastic spectroscopy of biomaterials," *J. Mech. Behav. Biomed. Mater.* **4**(7), 1115–1122 (2011).
- ³²B. Arnal, G. Pinton, P. Garapon, M. Pernot, M. Fink, and M. Tanter, "Global approach for transient shear wave inversion based on the adjoint method: A comprehensive 2D simulation study," *Phys. Med. Biol.* **58**(19), 6765–6778 (2013).
- ³³J. Virieux and S. Operto, "An overview of full-waveform inversion in exploration geophysics," *Geophysics* **74**(6), WCC1–WCC26 (2009).
- ³⁴E. Montagnon, A. Hadj-Henni, C. Schmitt, and G. Cloutier, "Rheological assessment of a polymeric spherical structure using a three-dimensional shear wave scattering model in dynamic spectroscopy elastography," *IEEE Trans. Ultrason. Ferroelectr. Freq. Control* **61**(2), 277–287 (2014).
- ³⁵E. Montagnon, A. Hadj-Henni, C. Schmitt, and G. Cloutier, "Viscoelastic characterization of elliptical mechanical heterogeneities using a semi-analytical shear-wave scattering model for elastometry measures," *Phys. Med. Biol.* **58**(7), 2325–2348 (2013).
- ³⁶J. J. Faran, "Sound scattering by solid cylinders and spheres," *J. Acoust. Soc. Am.* **23**(4), 405–418 (1951).
- ³⁷N. G. Einspruch, E. Witterholt, and R. Truell, "Scattering of a plane transverse wave by a spherical obstacle in an elastic medium," *J. Appl. Phys.* **31**(5), 806–818 (1960).
- ³⁸R. White, "Elastic wave scattering at a cylindrical discontinuity in a solid," *J. Acoust. Soc. Am.* **30**(8), 771–785 (1958).
- ³⁹F. Léon, F. Chati, and J. M. Conoir, "Modal theory applied to the acoustic scattering by elastic cylinders of arbitrary cross section," *J. Acoust. Soc. Am.* **116**(2), 686–692 (2004).
- ⁴⁰P. M. Morse and H. Feshbach, *Methods of Theoretical Physics* (McGraw-Hill, New York, 1953), Chap. 13, pp. 1762–1767.
- ⁴¹A. Hadj-Henni, C. Schmitt, and G. Cloutier, "Three-dimensional transient and harmonic shear-wave scattering by a soft cylinder for dynamic vascular elastography," *J. Acoust. Soc. Am.* **124**(4), 2394–405 (2008).
- ⁴²D. Cassereau, F. Mézière, M. Muller, E. Bossy, and A. Derode, "Computation of the diffracted field by an elliptic rigid or elastic scatterer: An overview of the numerical limitations," *Phys. Procedia* **70**, 208–212 (2015).
- ⁴³G. Montaldo, M. Tanter, J. Bercoff, N. Benech, and M. Fink, "Coherent plane-wave compounding for very high frame rate ultrasonography and transient elastography," *IEEE Trans. Ultrason. Ferroelectr. Freq. Control* **56**(3), 489–506 (2009).
- ⁴⁴D. Garcia, L. Le Tarnec, S. Muth, E. Montagnon, J. Porée, and G. Cloutier, "Stolt's f-k migration for plane wave ultrasound imaging," *IEEE Trans. Ultrason. Ferroelectr. Freq. Control* **60**(9), 1853–1867 (2013).
- ⁴⁵T. Loupas, R. Peterson, and R. W. Gill, "Experimental evaluation of velocity and power estimation for ultrasound blood flow imaging, by means of a two-dimensional autocorrelation approach," *IEEE Trans. Ultrason. Ferroelectr. Freq. Control* **42**(4), 689–699 (1995).
- ⁴⁶W. A. Berg, D. O. Cosgrove, C. J. Dore, F. K. Schafer, W. E. Svensson, R. J. Hooley, R. Ohlinger, E. B. Mendelson, C. Balu-Maestro, M. Locatelli, C. Tourasse, B. C. Cavanaugh, V. Juhan, A. T. Stavros, A. Tardivon, J. Gay, J. P. Henry, and C. Cohen-Bacrie, "Shear-wave elastography improves the specificity of breast US: The BE1 multinational study of 939 masses," *Radiology* **262**(2), 435–449 (2012).
- ⁴⁷A. Nabavizadeh, J. F. Greenleaf, M. Fatemi, and M. W. Urban, "Optimized shear wave generation using hybrid beamforming methods," *Ultrasound. Med. Biol.* **40**(1), 188–199 (2014).
- ⁴⁸A. Hadj-Henni, C. Schmitt, I. Trop, and G. Cloutier, "Shear wave induced resonance elastography of spherical masses with polarized torsional waves," *Appl. Phys. Lett.* **100**(13), 133702 (2012).